**Australian Bushfire Emissions Result in Enhanced Polar Stratospheric Ice Clouds**

Srinivasan Prasanth[1,2], Narayana Sarma Anand[3], Kudilil Sunilkumar[2], Subin Jose[4], Kenath Arun[1], Sreedharan K. Satheesh[2,5,6], and Krishnaswamy K. Moorthy[5]

[1]Department of Physics and Electronics, Christ University, Bengaluru, Karnataka, India

[2]Centre for Atmospheric and Oceanic Sciences, Indian Institute of Science, Bengaluru, Karnataka, India

[3]School of Earth, Environmental and Sustainability Sciences, Indian Institute of Science Education and Research Thiruvananthapuram, Kerala, India

[4]Department of Physics, Newman College, Thodupuzha, Kerala, India

[5]Divecha Centre for Climate Change, Indian Institute of Science, Bengaluru, Karnataka, India

[6]DST-Centre of Excellence in Climate Change, Indian Institute of Science, Bengaluru, Karnataka, India

*Correspondence*: Prasanth S. (prasanthphy57@gmail.com)

**Abstract**

Extreme bushfire events amplify climate change by emitting greenhouse gases and destroying carbon sinks while causing economic damage through property destruction and even fatalities. One such bushfire occurred in Australia during 2019/2020, injecting large amounts of aerosols and gases into the stratosphere and depleting the ozone layer. While previous studies focused on the drivers behind ozone depletion, the bushfire impact on the polar stratospheric clouds (PSC), a paramount factor in ozone depletion, has not been extensively investigated so far. This study focuses on the effects of bushfire aerosols on the dynamics and stratospheric chemistry related to the PSC formation and its pathways. An analysis from Aura's microwave limb sounder revealed enhanced hydrolysis of dinitrogen pentoxide significantly increased nitric acid ($HNO_3$) in the high-latitude lower stratosphere in early 2020. It resulted in anomalous high areal coverage of PSC with ice exceeding three standard deviations with respect to background period. Based on Lagrangian backward trajectory analysis, we report that 79 % and 21 % of liquid–Nitric Acid Trihydrate (NAT) mixture formed via ice-free and ice-assisted formation pathways respectively, and 95 % of ice formed via nucleating on NAT and rest on Supercooled Ternary Solution (STS) with possible inclusion of foreign nuclei. ~~Using a novel methodology which retrieves formation pathways of PSCs from spaceborne lidar observations, we found that the enhanced $HNO_3$ condensed on bushfire aerosols, forming 82 % of Liquid Nitric Acid Trihydrate (LNAT), which rapidly converted to 77 % of ice, resulting in an anomalous high areal coverage of ice PSCs.~~ This highlights the primary formation pathways of ice and ~~LNAT~~ liquid–NAT mixtures and possibly helps us to simulate the PSC formation and denitrification process better in climate models. ~~As tropospheric warming is anticipated to increase the frequency of extreme wildfire events and stratospheric cooling is expected to expand the PSC areal coverage, t~~These findings will contribute significantly to a deeper understanding of the impacts of extreme wildfire events on stratospheric chemistry and PSC dynamics.

**Keywords:** Aerosols; Australian Bushfire; Formation pathways; Polar Stratospheric Clouds; Stratospheric chemistry

## 1 Introduction

Southeast Australia, comprising the states of New South Wales and Victoria, faced an extreme bushfire event from September 2019 to February 2020, which is widely recognized as the black summer or Australian New Year (ANY) event and has been extensively studied (Allen et al., 2020; Deb et al., 2020; Schwartz et al., 2020; Chang et al., 2021; Rieger et al., 2021; Tencé et al., 2021, 2022; Heinold et al., 2022; Sellitto et al., 2022). This catastrophic event injected substantial amounts of aerosols, between 0.4 and 2 Tg, into the southern hemispheric lower stratosphere (Khaykin et al., 2020; Hirsch and Koren, 2021; Heinold et al., 2022; Tencé et al., 2022); which composed of 2.5 % black carbon and 97.5 % organic carbon (Yu et al., 2021). Significant warming of the mid-latitude stratosphere by up to 3.5 K has been reported, which is unparalleled since the 1991 eruption of Mount Pinatubo (Stocker et al., 2021). Additionally, this event led to significant changes in the abundance of various trace gas species, such as $CH_4$, CO, $CH_3CN$, $CH_3Cl$, HCN, $CH_3OH$, HCl, $HNO_3$, $H_2O$, and $ClONO_2$, particularly in the mid-latitude lower stratosphere (Schwartz et al., 2020; Santee et al., 2022; Wang et al., 2023).

Furthermore, these aerosols provided ~~a~~ surface area for heterogeneous chlorine activation reactions to occur, resulting in the early depletion of HCl and an enhancement of ClO (Santee et al., 2022a), and led to additional stratospheric ozone loss (Solomon et al., 2022). Along with these aerosols, liquid Polar Stratospheric Clouds (PSCs) are also known to promote such ozone-depleting heterogeneous reactions (Molina et al., 1993; Carslaw et al., 1994; Ravishankara and Hanson, 1996). Solid PSCs ~~like~~ such as Nitric Acid Trihydrate (NAT) are known to retard the deactivation process of active halogens like chlorine, bromine, and fluorine through denitrification and thereby contribute to prolonged ozone depletion (Hoyle et al., 2013). Ansmann et al. (2022) reported that the bushfire aerosols from the black summer event have influenced the PSCs by increasing their surface area and particle number concentration. Wang et al. (2023) reported an increased stratospheric chlorine activation on the bushfire aerosols and PSCs. However, previous studies have not extensively investigated the influence of the black summer event on the PSC dynamics, ~~specifically~~ particularly the formation pathways. It is ~~paramount~~crucial to understand the influence of extreme events like the black summer ~~event~~ on PSC dynamics for two main reasons:

(i) The frequency of extreme wildfire events is projected to increase due to global warming (Mansoor et al., 2022), resulting in more injection of aerosols into the stratosphere, which could enhance the PSC area coverage.

(ii) Stratospheric cooling is anticipated to further expand the PSC coverage, resulting in more surface area density for chlorine activation reactions and thus more ozone depletion (e.g., Khosrawi et al., 2016; Thölix et al., 2016; Robrecht et al., 2019).

Under the above backdrop, using multi-satellite measurements and reanalysis data, this study aims to investigate the anomalies in stratospheric chemistry and PSC dynamics caused by the black summer event.

~~The data and methodology used in this study are detailed in Sect. 2. The results and their discussion are given in Sect. 3 and the study is concluded in Sect. 4.~~

In this paper, we first review the polar stratospheric clouds and their formation pathways relevant to the current study in Sect. 2. The data and methodology used in this study are detailed in Sect. 3. The results and their discussion are given in Sect. 4 and the study is concluded in Sect. 5.

## 2. Brief literature review of Polar stratospheric clouds

The stratosphere contains ~~a~~ widespread presence of sulfate aerosols composed of sulfuric acid and water (Junge et al., 1961) which originate from sulfur emissions in the troposphere and ~~are transporits~~ transport to the stratosphere at a rate of 160 tons per day (Thomason and Peter, 2006). In addition to the~~se~~ sulfate aerosols, meteoritic dust particles of extraterrestrial origin contribute 20-100 tons per day (Cziczo et al., 2001; Curtius et al., 2005), making up 3–15% of the total mass of stratospheric aerosols. These dust particles are carried by the Brewer-Dobson circulation and funneled from the mesosphere into the stratospheric polar regions of both hemispheres during the formation of the polar vortex (Engel et al., 2013). As winter approaches, the absence of solar radiation in the polar regions leads to a significant decrease in temperature, creating conditions conducive for trace gases such as $HNO_3$ and $H_2O$ to condense onto the stratospheric aerosols, forming polar stratospheric clouds (PSCs) (Carslaw et al., 1994; Voigt et al., 2000). Hence, these PSC particles predominantly consist of $HNO_3$, $H_2SO_4$, and $H_2O$ (Lowe and MacKenzie, 2008; Peter, 1997). It is hypothesized that stratospheric sulfuric acid aerosols containing meteoritic dust could also serve as the nuclei for PSC formation (Bogdan et al., 2003; Bogdan and Kulmala, 1999; Murphy et al., 2014; Schneider et al., 2021).

### 2.1 Types of PSC

The PSCs exist in both liquid and solid form in the lower stratosphere. The Supercooled Ternary Solution (STS) is liquid PSC with an equal proportion of $H_2SO_4$, $HNO_3$, and $H_2O$ which forms at $T_{ice}$ + 3 K (Carslaw et al., 1994). The Nitric Acid Trihydrate (NAT) particles always exist in the solid phase with a proportion of 1 $HNO_3$ and 3 $H_2O$ and form at $T_{ice}$ + 7 K (Hanson and Mauersberger, 1988). Furthermore, ice PSC forms through homogeneous nucleation at $T_{ice}$ – 4 K (Carslaw et al., 1998), and heterogeneous nucleation of ice at $T_{ice}$ – 0.1 to 1.3 K (Fortin et al., 2003). Among the different types of PSCs, liquid forms such as STS, as well as other liquid stratospheric aerosols provide a surface for chlorine activating heterogeneous chemical reactions and play an important role in ozone destruction (Molina and Rowland, 1974; Molina et al., 1993; Ravishankara and Hanson, 1996). The active form of chlorine is deactivated by $NO_y$ species. But the solid PSC like NAT grows large in size, typically > 10 µm, and undergoes a gravitational settling process, leading to permanent removal of NOy. This process, known as denitrification, prevents the deactivation of chlorine and other halogens, thereby prolonging ozone depletion (Hoyle et al., 2013; Waibel et al., 1999).

## 2.2 PSC formation pathways

### 2.2.1 NAT formation pathways

The homogeneous nucleation of NAT is kinetically suppressed (Koop et al., 1995). Laboratory experiments have revealed that the homogeneous nucleation rate of NAT on liquid STS is extremely low for stratospheric conditions (Hanson and Ravishankara, 1991; 1992). Thus, NAT forms through heterogeneous nucleation processes such as (i) ice–assisted NAT nucleation and (ii) ice-free NAT nucleation. During the ice–assisted NAT nucleation process, the ice particles serve as nuclei for NAT formation upon warming and it occurs at a high saturation ratio over NAT of > 500 (Luo et al., 2003). This mechanism has been supported by several field observations (Carslaw et al., 1999) and by bulk phase lab experiments (Koop et al., 1995, 1997) indicating that deposition nucleation of NAT on exposed ice surfaces is also a possible pathway for NAT formation. During the ice-free NAT nucleation, instead of ice, STS with inclusion of solid foreign nuclei such as meteoritic dust, volcanic ash, soot, or $H_2SO_4$ hydrates serve as NAT nuclei (Iraci et al., 1995; Koop et al., 1997; Peter and Grooß, 2012) and it occurs during the low saturation ratio over NAT ($S_{NAT}$) of < 10 (Voigt et al., 2005). Ground-based lidar observations by Biele et al. (2001) provided evidence of the existence of such STS with foreign nuclei inclusion. Hoyle et al., 2013 made a new parameterization scheme for NAT nucleation on foreign nuclei in immersion mode and reproduced the CALIPSO PSC observation for the entire Arctic winter 2009/2010.

### 2.2.2 Ice formation pathways

The ice PSC can form either homogeneously under high supersaturation conditions of saturation ratio over ice ($S_{ice}$) >1.5 and at temperature 3 K less than the frost point ($T_{ice}$) (Koop et al., 1998) or heterogeneously on STS with foreign nuclei inclusion at temperature 1.5 K less than $T_{ice}$ (Koop et al., 1998; 2000; Engel et al., 2013). Apart from these foreign nuclei, the NAT is also known to act as potential nuclei for ice formation (Gao et al., 2016; Hanson and Mauersberger, 1988; Iannarelli and Rossi, 2015; Khosrawi et al., 2011; Weiss et al., 2016). Based on WALES (Water Vapor Lidar Experiment in Space – airborne demonstrator) lidar on board, the HALO (High Altitude and Long Range Research Aircraft), Voigt et al., al (2018) showed that the depolarization ratio of ice PSC exhibited bimodal distribution where low depolarization mode corresponds to the ice nucleated on STS with foreign nuclei inclusion and high depolarization mode to the ice nucleated on NAT particle. Engel et al., (2013) made a new parameterization scheme for ice nucleation on foreign nuclei in immersion mode and reproduced the CALIPSO PSC observation for the entire Arctic winter 2009/2010.

In the present study, along with investigating the impact of black summer event on lower stratospheric chemistry, we also aim to quantify the percentage of the liquid-NAT mixture formed via ice-assisted and ice-free nucleation process. Further, we quantity percentage of ice PSC which nucleates on NAT (NAT-assisted nucleation pathway), and STS (NAT-free nucleation pathway). Note that the NAT can form only through a heterogeneous nucleation process under lower stratospheric conditions, and hence STS should have solid foreign nuclei included within for a NAT-free nucleation pathway to occur.

## ~~2~~ 3 Data and Methodology

### ~~2~~3.1 Satellite and reanalysis data ~~Satellite data~~

Ozone Monitoring Profiler Suite (OMPS) on board Suomi NPP and NOAA-20 satellites measures atmospheric $O_3$ and aerosols using limb viewing techniques. We have used OMPS level 2 version 2.0 product which provides aerosol extinction coefficient at 745 nm wavelength, with a horizontal resolution of 125 km × 2 km and a vertical resolution of 1.8 km (https://disc.gsfc.nasa.gov/datasets/OMPS_NPP_LP_L2_AER_DAILY_2/summary; Taha et al., 2021).

Microwave Limb Sounder (MLS) aboard the Aura satellite provides the trace gas~~es~~ mixing ratios by measuring limb emission spectra through ~~a 5-band microwave radiometer a Fourier Transform Spectrometer (FTS)~~. We have used ~~T~~the MLS Level 2, version 5.0 daily $HNO_3$ and $H_2O$ mixing ratios ~~are used~~ (https://mls.jpl.nasa.gov/eos-aura-mls/data-products; Waters et al., 2006) for the present study~~.~~

Atmospheric Chemistry Experiment-FTS (ACE-FTS) onboard SciSat satellite provides trace gases mixing ratio by measuring limb absorption spectra and level 2, version 4.0 daily HF, $H_2O$, $HNO_3$, $N_2O_5$ mixing ratio (https://www.frdr-dfdr.ca/repo/dataset/c75d2c49-0def-49e5-9c69-5e74c824dc6c; Bernath et al., 2020). ~~are used in the present study~~.

Cloud-Aerosol Lidar with Orthogonal Polarization (CALIOP) onboard the Cloud-Aerosol Lidar and Infrared Pathfinder Satellite Observations (CALIPSO) satellite probes the vertical distribution of aerosols and clouds. ~~The PSCs are detected as those measurements with a relatively larger extinction coefficient than the background aerosol extinction coefficient~~ (Pitts et al., 2007). ~~-~~It classifies the ~~detected PSCs~~PSCs through perpendicular attenuated backscatter and total scattering ratio (ratio between the total attenuated backscatter to the molecular backscatter), into five categories: Supercooled Ternary Solution (STS ≡ $H_2SO_4.HNO_3.H_2O$), Liquid ~~-~~Nitric Acid Trihydrate mixtures (liquidNAT mixtures~~LNAT~~ ≡ $HNO_3.3H_2O$, a mixture of liquid STS and solid NAT with low number density of $10^{-2}$ $cm^{-3}$), ~~ENAT~~ enh. NAT (Enhanced NAT, with a high number density of $10^{-1}$ $cm^{-3}$), Ice (Water ice ≡ $H_2O$), and Mountain Wave Ice (MWI ≡ $H_2O$, caused by gravity waves). The total areal coverage of the PSCs such as liquid—NAT mixtures~~LNAT~~, STS, Ice, ~~ENAT~~enh. NAT~~,~~ and MWI contribute~~s~~ to 48 %, 24.7 %, 21.4 %, 5.8 %, and 0.1 % respectively (Pitts et al., 2018). In addition, gas-phase $HNO_3$ is observed from Microwave Limb Sounder (MLS) from March to April every year. The backscattered signals from the sub-visible PSCs, which are NAT particles with extremely low number density, are well below the detection threshold of the CALIPSO receiver. Hence CALIPSO classifies these grids as 'No Cloud (NC)' (Lamber et al., 2012) during this period. Thus, the CALIPSO NC grid indicates either no presence of PSC or the presence of sub-visible PSC. In this study, CALIPSO PSC Level 2, version 2.0 is used (https://asdc.larc.nasa.gov/project/CALIPSO/CAL_LID_L2_PSCMask-Standard-V2-00_V2-00; Pitts et al., 2007; 2009; 2013), which provides PSC information at a spatial resolution of 180 m (vertical) × 5 km (horizontal). The PSC areal coverage is estimated as described in Pitts et al. (2009).

European Centre for Medium-Range Weather Forecasts Reanalysis fifth generation (ERA-5) reanalysis provides meteorological data with a spatial resolution of 0.25° × 0.25° and a temporal resolution of 1 hour at 37 pressure

levels (1000 to 1 hPa). We have used the hourly meridional and zonal velocity from June 2020 to July 2020 (https://cds.climate.copernicus.eu/cdsapp#!/dataset/reanalysis-era5-pressure-levels?tab=overview; Hersbach et al., 2020).

### ~~2~~3.2 Anomaly estimation

Anomalies (Δ) in aerosol extinction coefficient ($k_{ext}$ at 745 nm), mixing ratios of $H_2O$, and $HNO_3$, and PSC properties are estimated following Eq. (1):

$$\Delta X = X_{2020} - \bar{X} \quad (1)$$

where 'ΔX' is a daily anomaly of quantity 'X', '$X_{2020}$' is the daily mean in 2020, and '$\bar{X}$' is the daily background mean. The background mean values of $H_2O$ and $HNO_3$ mixing ratio and PSC properties are constructed by averaging the daily values during the period 2009 to 2019 while for $k_{ext}$, the period is 2012 to 2019 [excluding the year 2015, to avoid the effects of the Calbuco volcanic eruption (Zhu et al., 2018)]. The standardized anomaly (Z) is estimated following Eq. (2):

$$Z_X = \frac{\Delta X}{\sigma_X} \quad (2)$$

where '$\sigma_X$' is the standard deviation of the parameter 'X'.

### ~~2~~3.3 Methodology for ~~Retrieval~~ retrieval of formation pathways

~~The CALIPSO PSV v2.0 product provides just information about the presence of PSCs and their types but no information about their respective formation pathways.~~ To retrieve the formation pathways of the PSCs, knowledge of the temperature history of the corresponding air parcel is crucial (Larsen et al., 1997). Hence, using the CLaMS trajectory module, the backward trajectories of the air parcels containing ice and liquid NAT mixture PSCs are calculated. The methodology ~~that retrieves the PSC formation pathways from CALIPSO has been discussed earlier~~ is similar to the previous studies which retrieved the PSC formation pathways from CALIPSO (Nakajima et al., 2016) and from aircraft campaigns (Voigt et al., 2018) using Lagrangian trajectory analysis. The current methodology employed in this paper has three sections: (i) Selection of ice and liquid NAT mixture PSCs, (ii) Lagrangian backward trajectory analysis, and (iii) Determining the change in PSC composition. These three sections are described below.

*(i) Selection of ice and liquid-NAT mixture PSCs:* Since liquid-NAT mixture and ice are the first (with 48 %) and third (with 21.4 %) most abundant types of PSCs in terms of areal coverage (Pitts et al., 2018), performing backward trajectories for all these detected PSC types is computationally expensive. Furthermore, The ERA5 operational analysis data are available at the temporal resolution of 1 hr. Whereas, the CALIPSO's temporal resolution is 1 profile $sec^{-1}$. The accuracy of the trajectory relies on the accuracy of the wind field and diabatic heating rate. Hence, assigning hourly wind field and diabatic heating rate to all CALIPSO profiles measured during the specific hour may contribute to uncertainty in the calculated trajectory. Though the degree of uncertainty is unclear, as a conservative measure, we impose another criterion to minimize any uncertainty which may contribute.

Criteria 1: Firstly, CALIPSO profiles which are measured within 5 minutes before and after (i.e., the 10-minute time windows) of any hours of ERA5 operational analysis are chosen. For instance, if ERA5 operational analysis data is available for the time 01:00 UTC for a specific day, CALIPSO profiles which are measured between 12:56 UTC and 01:05 UTC on the same day are considered.

Criteria 2: Secondly, from these chosen profiles, an ice PSC (liquid-NAT mixture PSC) grid is chosen only if all its surrounding grids are classified as ice PSC (liquid-NAT mixture PSC) i.e., the CALIPSO grids of size 3x3 should be homogeneously populated by either ice or liquid-NAT mixture.

*(ii) Lagrangian backward trajectory analysis:*

The backward trajectories for these selected grid points are calculated for a 48 h period using the CLaMS trajectory module. The rationale behind choosing the 48 h is that once the air parcel's temperature drops below $T_{NAT}$ and following the nucleation of NAT particles with a number density of $5\times10^{-4}$ to $5\times10^{-5}$ $cm^{-3}$, within ~19 h (0.8 day) the NAT particles exceed CALIPSO perpendicular backscatter threshold and becomes detectable (Lambert 2012). Similarly, Voigt et al. (2005) provided observational evidence from aircraft campaigns showing NAT formation within approximately 20 hours after the temperature drops below $T_{NAT}$. In the case of ice formation, the 48 h period should be sufficient while considering the average cooling rate of the stratosphere. The model runs are driven by meteorological data from the ERA5 operational analysis, with a temporal resolution of 1 hour and a spatial resolution of 1° x 1°. The timestep is set to 60 seconds in the CLaMS trajectory module. The vertical coordinate is in potential temperature. The vertical motion of the air parcels is modulated by total diabatic heating rates derived from ERA5 as followed by Ploeger et al., (2021).

*(iii) Determining the change in PSC composition*

To determine the PSC composition along each trajectory, we first identify the intersection points where the trajectory intersects with the CALIPSO scan track, with a temporal coincidence of ±30 minutes. Intersections with time differences exceeding this threshold are disregarded, ensuring that the trajectory and CALIPSO scan track are both spatially and temporally co-located within a 30-minute time window. The PSC composition at each trajectory intersection point is then determined from the CALIPSO measurement profile with a potential temperature closest to that of the trajectory's intersecting point. If the determined PSC composition in this manner differs from the initial composition observed at the start of the trajectory (i.e., at time t = 0 h), we assign this PSC composition to the intersection point of the trajectory. Conversely, trajectories with no change in PSC composition are excluded from further consideration.

By applying this process, we fill all the trajectories with CALIPSO PSC compositions, providing a comprehensive picture of the air parcel's temporal evolution and the subsequent formation of NAT and ice.

### 3.4 Microphysical modelling of observed uptakes of $HNO_3$ and $H_2O$

During the formation of ice and liquid-NAT mixture PSCs, uptake of gas-phase $HNO_3$, and $H_2O$ mixing ratio occurs. Using the CLaMS microphysical box model, we validated the modeled uptake of $HNO_3$ and $H_2O$ mixing ratio against the MLS observed uptake of these gases. For this, the trajectories are fed into the CLaMS box model along with the MLS observed $HNO_3$, and $H_2O$ at the beginning of the trajectory. In the box model run, $T_{ice}$ is

estimated following equations provided by Hanson and Mauersberger (1988), and $T_{NAT}$ is estimated following Hanson and Mauersberger (1998).

~~CALIPSO provides PSC composition derived from the backscattered signal, but it does not carry information about Lagrangian trajectory analysis but were limited to a few days. However, the methodology they employed did not provide a relative percentage contribution of various formation pathways of PSCs. We have developed a new methodology to address this limitation.~~

~~The CALIPSO orbits the Earth ~15 times per day with an orbit period of ~100 minutes. These scan tracks periodically intersect at high latitude regions (an example is given in Fig. 1a). The intersection points provide a unique opportunity to measure the PSC composition at certain intervals of time. In this study, we choose the intersection between the scan 'n' and scan '(n+2)' which usually occurs at latitude ~ 80°. The time interval between these two scans is ~200 minutes. Though we have a measurement of the PSC composition at the same location with a periodic time interval, the air parcel tends to move vertically and horizontally. Hence, it is vital to find the distance traveled by air parcels in the given 200 minutes. The vertical velocity of the air parcel at the lower stratosphere is extremely low of order of 0.001 m s$^{-}$ horizontal velocity varies according to the prevailing meteorological condition modulated by the polar vortex.~~

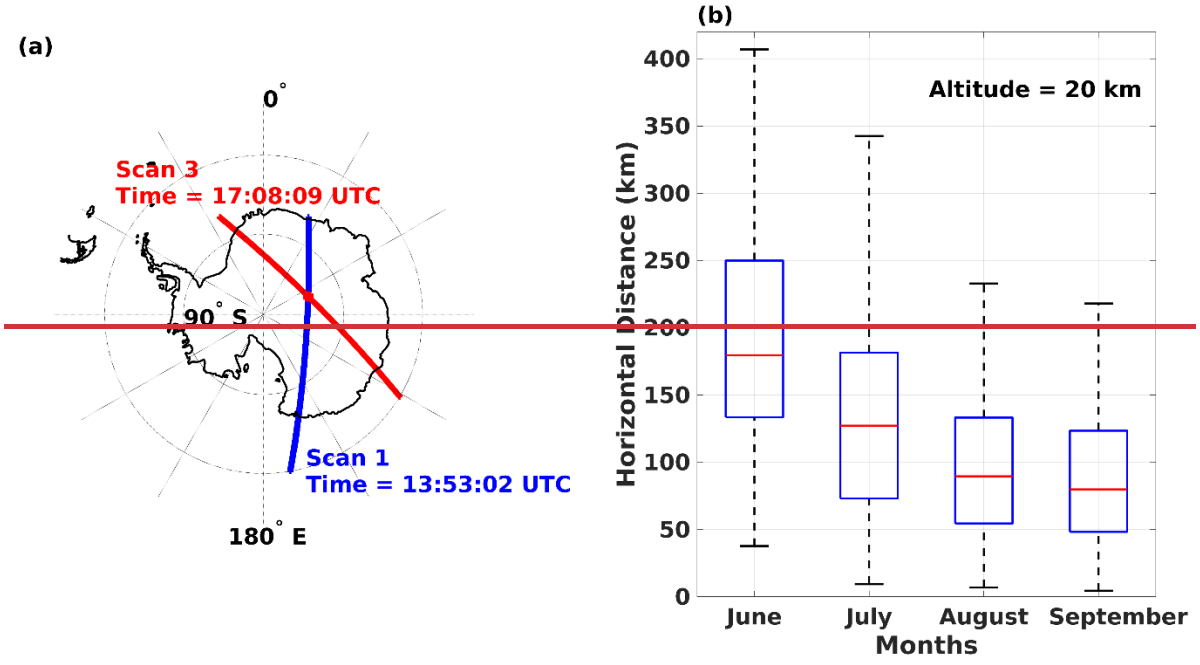


~~*Figure 1: (a) Intersection of two CALIPSO scan tracks: Scan 1 (blue line) and Scan 3 (red line) during 01/08/2020 and (b) Boxplot showing the simulated horizontal distance traveled by air parcels for 240 minutes starting at 00:00 (hour: minutes) at an altitude of 20 km during June, July, August, and September of 2020. In the boxplot, the redline marks the median distance, the horizontal blue lines below and above the median mark the first and third quartile respectively, and the lower and uppermost black lines mark the minimum and maximum distance traveled by the air parcels.*~~

To find the horizontal distance traveled by the air parcels, we utilized a trajectory module from the Chemical Lagrangian Model of the Stratosphere (CLaMS) where the ERA5 hourly meteorological dataset is provided as an input. For the simulation, the initial location of the air parcels is considered to be at latitude ~80°, time 00:00 UTC (hh: mm), longitude between 0° and 360° at an interval of 45° and altitude of 20 km. The air parcels are allowed to travel for the next 4 hours (240 mins) in the trajectory module. Though the requirement is to measure the horizontal distance traveled by air parcels in 200 minutes, we run the trajectory module on an hourly scale to reduce the computational cost. Hence, the monthly statistics of the distance traveled by the air parcels in 240 minutes, starting from the initial location, are shown in Fig. 1b.

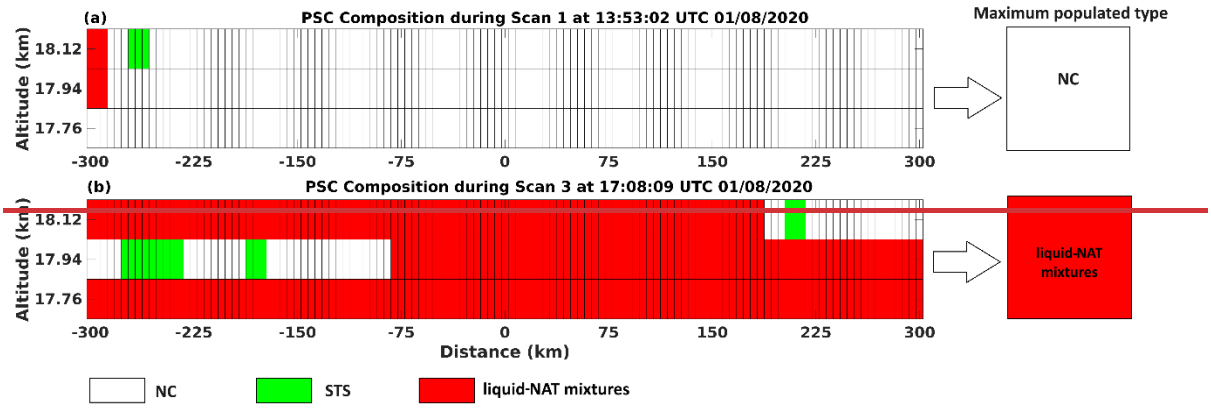


*Figure 2: Observed CALIPSO PSC composition during 01/08/2020 at (a) Scan 1 and (b) Scan 3. The '0 km' in the x-axis marks the intersection of the two scan tracks. 'NC', 'LNAT', and 'STS' stand for No Cloud (white), Liquid Nitric Acid Trihydrate (red), and Supercooled Ternary Solution (green).*

Based on the trajectory results, it is found that the monthly mean distance traveled by the air parcels is within 300 km. Hence, around the intersection, profiles falling within a 300 km radius and three consecutive vertical levels (i.e., 540 m) are chosen, as shown in Fig. 2. The maximum populated PSC within the chosen boundary is assumed to be the PSC of the air parcel. This reclassification reduces the noise further. The transition in the maximum populated PSC type during the two scans provides vital information about the PSC formation pathways. In CALIPSO PSC Version 2.0, statistical threshold values of perpendicular attenuated backscatter ($\beta_{\perp}$) and total scattering ratio ($R_{532}$) are used to classify the PSC composition, the perpendicular attenuated backscatter refers to the perpendicular component (i.e., polarization perpendicular to the emitted lidar signal) of the attenuated backscatter signal from the particulate and the total scattering ratio is the ratio between the total particulate backscatter and molecular backscatter. For example, the particle is classified as enhanced NAT PSC if it's $2 < R_{532} < 5$ and $\beta_{\perp} > 2\times10^{-5}$ km$^{-1}$ sr$^{-1}$, as ice PSC if it's $2.75 < R_{532} < 50$ and $\beta\perp >\sim 1.55\times10^{-5}$ km$^{-1}$ sr$^{-1}$ and STS PSC if it's $\beta\perp < \sim 1.55\times10^{-5}$ km$^{-1}$ sr$^{-}$, the other types of PSCs are classified based on empirically found threshold values. More details can be choose PSCs whose optical properties are far away from these thresholds (i.e., more than one standard deviation with respect to the threshold value). Through this, we ensure that only grids which exhibited drastic change in PSC optical properties during the 200 minutes are considered for the retrieval of PSC formation pathways. It should be noted that as these intersections occur at the latitude of ~ 80°, the retrieved

formation pathways correspond to the interior of the polar vortex. As such, they cannot be considered representative of all PSC formations which occur outside the polar vortex.

The CALIPSO PSC composition observed on 01/08/2020 in Scan 1 and Scan 3 are shown in Fig. 2. The horizontal and vertical boundaries are selected as described above. During Scan 1, No Cloud (NC) is the maximum populated PSC type (NC refers to the presence of no clouds as observed by CALIPSO but may contain stratospheric aerosols/sub-visible PSC/NAT, all grids within this boundary are labeled as 'NC. During scan 3, as LNAT is the maximum populated PSC type, it is traced that "NC" turned into "LNAT" in the given ~200 minutes. Similarly, all possible formation pathways of both ice and LNAT are retrieved during each successful intersection point. This technique helps us to narrow down the possible formation pathways. However, it is difficult to uniquely conclude the formation pathways using CALIPSO PSC information only. Because, as discussed earlier, 'NC' refers to the air parcel containing either stratospheric aerosols or large NAT rock, whose optical properties are below the CALIPSO detection threshold. If the same air parcel became populated with 'LNAT' after a certain time, it could imply that it either formed through nucleation on stratospheric aerosols aided by decreased temperature or evaporation of large NAT rock aided by increased temperature such that its size now falls within CALIPSO detection thresholds. Hence, to conclude which formation pathway is responsible for the specific PSC formation, it is essential to consider the corresponding change in temperature and gaseous species also, as described in the next section.

### 2.4 Thermodynamic Analysis of PSC Formation Pathways

The change in air temperature and gas phase $HNO_3$ mixing ratio offer valuable insight into potential PSC formation pathways, as described in Sect. 2.3, we accounted for changes in these parameters when retrieving the PSC formation, each formation pathway occurs at a specific temperature, which is conventionally viewed in the 'T-$T_{ice}$' temperature. Here 'T' is the ambient air temperature and '$T_{ice}$' is the frost point. The estimation of '$T_{ice}$' follows the parameterization described e change in air temperature 'ΔT', and gas phase nitric acid '$\Delta HNO_3$' are estimated following Eqs. (3) and (4) respectively.

$$\Delta T = T_n - T_{n+2} \quad (3)$$

$$\Delta HNO_3 = HNO_{3_n} - HNO_{3_{n+2}} \quad (4)$$

where $T_n$ and $HNO_{3_n}$ respectively represent the temperature and $HNO_3$ mixing ratio of the air parcel during the scan 'n'. The temperature and $HNO_3$ are obtained from MLS and MERRA-2 (provided along with CALIPSO PSC v2.0 product) respectively. For reliable results, the estimated ΔT and $\Delta HNO_3$ (using Eqs. 3 and 4) should be statistically significant such that their magnitude should be higher than their respective measurement uncertainties. The measurement uncertainty (represented by σ) in temperature and $HNO_3$ is 0.5-0.6 ppbv respectively. Hence, the combined uncertainty in ΔT and $\Delta HNO_3$ are estimated following the summation in quadrature

$$\sigma(\Delta x) = \sqrt{2\sigma(x)^2} \quad (5)$$

Where '$\sigma(\Delta x)$' represents the uncertainty in $\Delta x$, and '$x$' represents the $HNO_3$ mixing ratio or T. Similarly, the uncertainty in 'T-$T_{ice}$' is estimated following Eq. (6):

~~$\sigma(T - T_{ice}) = \sqrt{(\sigma(T)^2 + \sigma(T_{ice})^2}$ (6)~~

~~Where $\sigma(T_{ice})$ is the uncertainty in $T_{ice}$ which is taken as 0.5 K (Lambert et al., 2016). To ensure the reliability of the results, we are excluding values of $\Delta T$, $\Delta HNO_3$, and $T - T_{ice}$ falling within the respective uncertainty limits $\sigma(T)$, $\sigma(HNO_3)$, and $\sigma(T - T_{ice})$.~~

## ~~3~~4 Results and discussions

### ~~3~~4.1 Increased aerosol loading in the lower stratosphere

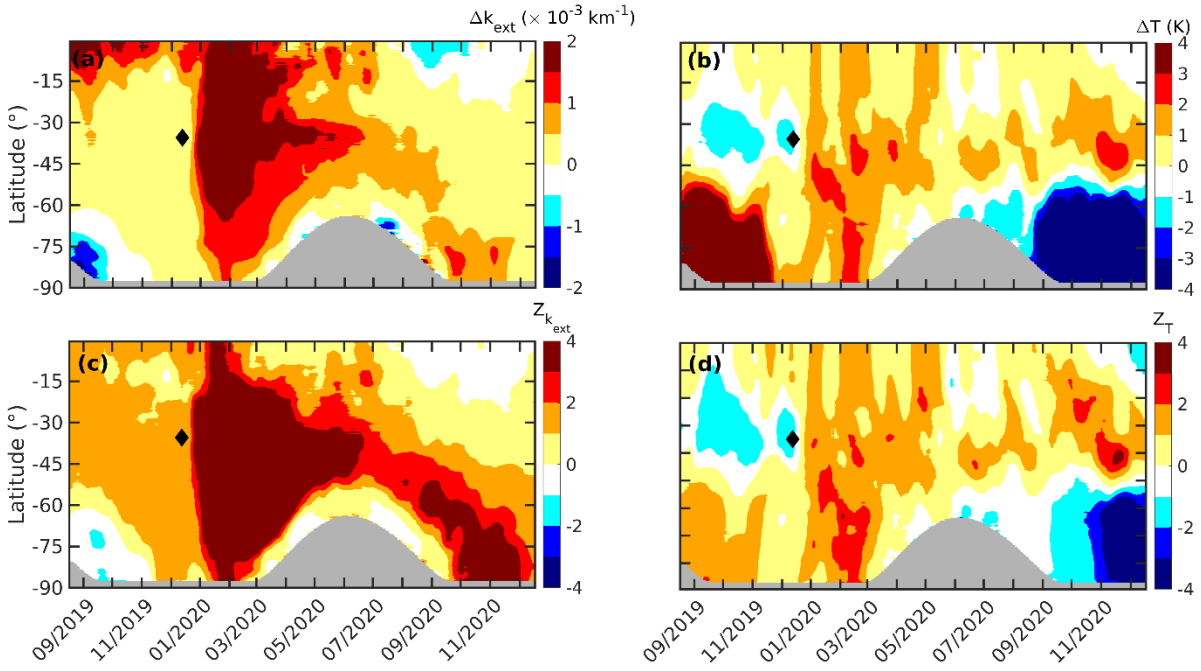


*Figure ~~3~~1: Daily zonal mean anomaly (Δ) in OMPS (a) $k_{ext}$ at 745 nm, (b) temperature, and standardized anomaly (Z) of (c) $k_{ext}$ at 745 nm and (d) temperature at the altitude of 15 km between September 2019 and December 2020 are shown. The grey-shaded region corresponds to no data. The x-ticks mark the middle of each month. The black diamond in each plot marks the black summer event.*

An anomaly in aerosol extinction coefficient ($k_{ext}$) at 745 nm derived from cloud-filtered OMPS observations, and temperature along with their corresponding standardized anomalies at the altitude of 15 km are shown in Fig. 1~~3~~. A notable positive anomaly of $k_{ext}$ in mid-latitude since early January 2020 is attributable to the increased aerosol loading caused by the black summer event (Fig. ~~3~~1a). The anomaly in $k_{ext}$ exceeded three standard deviations (Fig. ~~3~~1c) and warmed the lower stratosphere by 2 K owing to the radiative heating (Rieger et al., 2021), which is readily seen in Fig. ~~3~~1b. By February 2020, these aerosols have been transported to high latitudes where PSC usually forms in the subsequent Austral winter. As stratospheric aerosols act as nuclei for PSC, it is likely that these aerosols also influenced the PSC dynamics during this period. A negative anomaly of $k_{ext}$ has been observed at the latitude ~-80° since April 2020, which is attributed to the nucleation of PSC on these aerosols (Zhu et al.,

2018). The $k_{ext}$ increased again at high latitudes in October and November 2020 due to the re-release of the captured aerosols by the PSC, upon evaporation of the corresponding gas species (Toon et al., 1989; Schwarzenböck et al., 2001; Rex et al., 2004; Hoyle et al., 2013). Previous studies reported additional ozone loss during the same period (Ansmann et al., 2022; Ohneiser et al., 2022). Despite the abundant aerosol loading, strong cooling of more than 3 K is observed at high latitude regions from September to December 2020 (Fig. ~~3~~1b). This suggests that the radiative cooling caused by the additional ozone loss (Fig. S1) has surpassed the radiative heating by the increased aerosol loading, in agreement with Rex et al., (2004). Before the black summer event, intense warming exceeding 5 K was observed at the high latitude of the lower stratosphere from September to November 2019, which was attributed to a minor sudden stratospheric warming event (Liu et al., 2022).

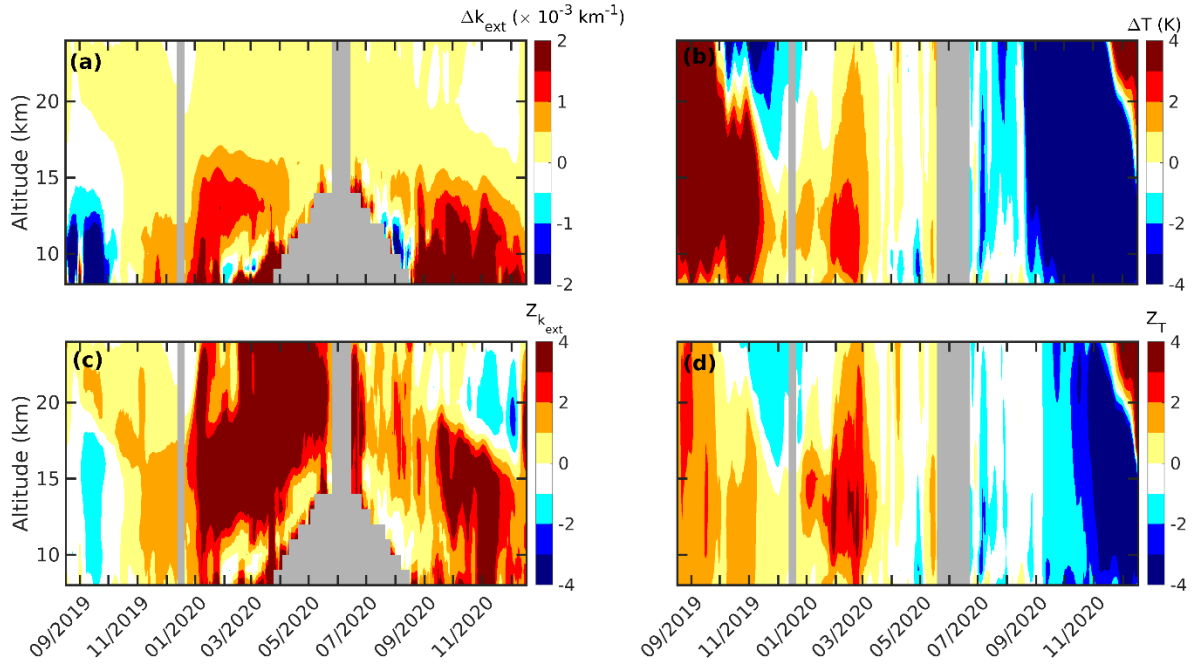


*Figure ~~4~~2: Daily vertical anomaly (Δ) in OMPS (a) $k_{ext}$ at 745 nm, (b) temperature, and standardized anomaly (Z) of (c) $k_{ext}$ at 745 nm and (d) temperature averaged between latitude -60° and -90° from September 2019 to December 2020 are shown. The grey-shaded region corresponds to no data. The x-ticks mark the middle of each month. The black diamond in each plot marks the black summer event.*

The vertical profiles of anomaly and standardized anomaly (Z) of $k_{ext}$ and temperature are shown in Fig. ~~4~~2. Significant aerosol loading is observed as shown in Fig. ~~4~~2a between the altitudes of 10 to 25 km from January to June 2020. The continuous increase in $Z_{kext}$ since January 2020, to an even higher altitude (Fig. ~~4~~2c), is attributed to the self-lofting mechanism (Khaykin et al., 2020). Like Fig. ~~1~~3, the positive anomaly in $k_{ext}$ in the lower stratosphere from October to December 2020 surpassed the anomaly observed during early 2020. The major type of aerosol emitted during the black summer is organic carbon (Yu et al., 2021), which is hydrophilic in nature. The increased $k_{ext}$ could hence be due to the exposure of these aerosols in the low temperatures during the winter where condensation of water vapor resulted in the growth of the aerosols, increasing its size and light extinction further. In addition, the transport of more bushfire aerosols from mid to high latitude regions could be another

cause of the observed increase in $\Delta k_{ext}$. The descending pattern as observed in $Z_{kext}$ (Fig. 42c) from August to December 2020 could be due to the result of the descent of the mesospheric air, as explained by Kessenich et al. (2023).

These observations reveal high aerosol loading in the lower stratosphere of the high latitudes after the black summer event. It can increase the surface area availability for heterogeneous chemical reactions and potentially modify the stratospheric chemistry itself. For a comprehensive understanding of the impact of the black summer event on the PSC dynamics, we explore the changes in key constituent gases of PSCs in the next section.

### 34.2 Enhanced $HNO_3$ and $H_2O$ in the lower stratosphere

The anomalies in MLS $HNO_3$ and $H_2O$ mixing ratios along with their corresponding standardized anomalies averaged between latitudes -60° and -90° are shown in Fig. 53. An elevated level of $HNO_3$ mixing ratio has been observed between 20 to 30 km altitude since February 2020 and peaked by 1.5 ppb over the background value by April 2020 (Fig. 53a). This surge exceeded two standard deviations and remained significant till June 2020 at the altitude of 20 km (Fig. 53c). Similarly, an increase in the $H_2O$ mixing ratio is observed at slightly lower altitudes (between 15 to 20 km) since mid-January 2020 (Fig. 53b), which exceeded more than one standard deviation (the cause of this anomalous increase is discussed in Sect. 3.3). As both $HNO_3$ and $H_2O$ are principal constituents of the PSCs (Höpfner et al., 2006; Tabazadeh et al., 1994; Tritscher et al., 2021; Voigt et al., 2000), the near-simultaneous decrease of them along with $k_{ext}$ (Fig. 42a) during Austral winter suggests that these species condensed on the bushfire aerosols and thus likely converted into PSCs.

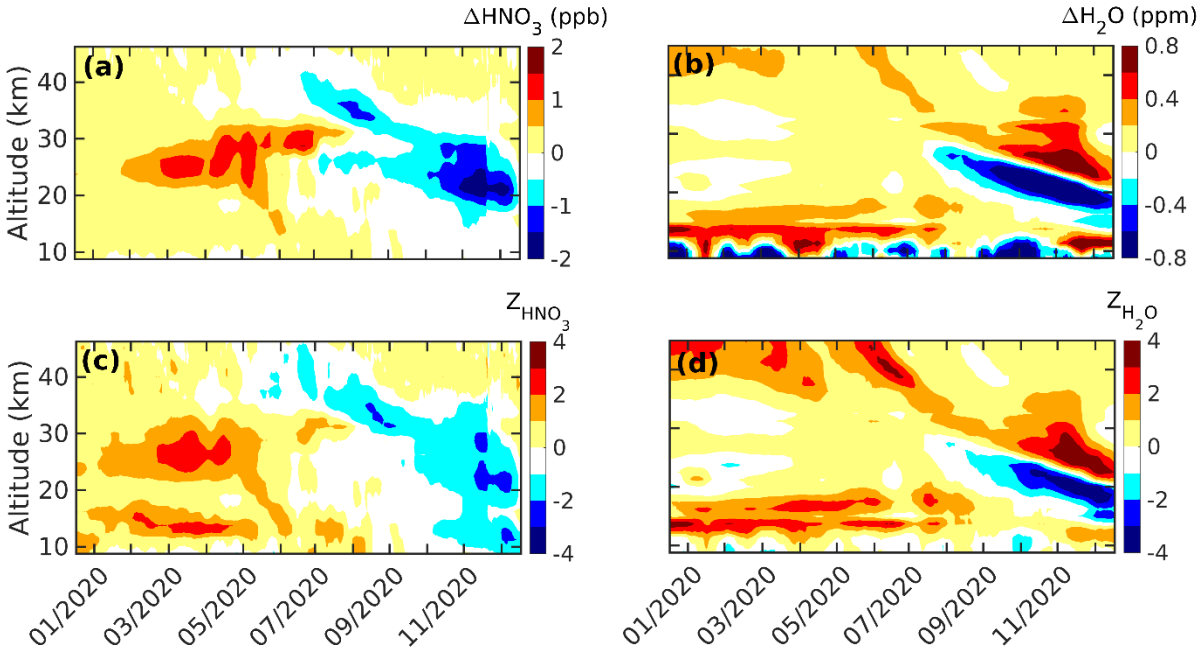


*Figure 53: Anomaly in (a) $HNO_3$ and (b) $H_2O$ mixing ratio, and standardized anomaly of (c) $HNO_3$ and (d) $H_2O$ mixing ratio, averaged between latitudes -60° and -90° during 2020. The x-ticks mark the middle of each month.*

Unlike $HNO_3$, abundant water vapor is detected in the upper stratosphere (above 40 km) (Fig. 53b and d) from January to April 2020. Since there is no evidence that the smoke plume from the black summer event has reached

such altitudes, we believe that the moist upper stratosphere is not associated with the black summer event. The upper stratospheric water vapor is produced through the oxidation of methane $CH_4$ (Brewer, 1949; Fueglistaler et al., 2009) and directly injected from the tropical tropopause layer through deep convection (Schoeberl et al., 2018). This water vapor is further transported from low to high latitudes through a deep branch (present at the upper and middle stratosphere) and a shallow branch (present just above tropopause) of the Brewer-Dobson circulation (Butchart, 2014). The descent of water vapor from the upper stratosphere to the lower stratosphere during 2020 shown in Fig. ~~5~~3b suggests that these water vapors are carried by the deep branch of the Brewer-Dobson circulation and resulted in a strong positive $H_2O$ anomaly from September to December 2020 within the altitudes of 30 to 25 km. A strong negative anomaly in both $HNO_3$ and $H_2O$ can be observed below this layer during early 2020, which could be due to the prolonged polar vortex during this period separating the mid and high-latitude air mass, thereby preventing further mixing (Rieger et al., 2021; Klekociuk et al., 2022; Santee et al., 2022b; Yook et al., 2022). To understand whether the cause of these anomalies was due to dynamical (i.e. due to change in transportation) or chemical (i.e., due to chemical reaction) processes, a tracer-tracer correlation analysis was carried out and the results are discussed in the next section.

### ~~3~~4.3 Tracer-Tracer Correlation Analysis

The Tracer-~~T~~tracer correlation analysis technique is used to diagnose whether a change in atmospheric gas concentration is driven by chemical reactions or transportation (such as convection or advection). The idea behind this technique is that chemically active and long-lived trace~~r~~ (i.e., chemically inert) gas should exhibit the same order of change if the cause is transport-related (e.g., Müller et al., 1996, 1997). If a chemically active gas increases/decreases with no change in long-lived trace~~r~~ gas, that change is attributed to the chemical reaction. In this technique, a linear regression between the long-lived trace~~r~~ gas and the chemically active gas is performed for both during the background periods (in this study, March 2009–2019). A deviation of the data corresponding to the period of interest (March 2020; red diamond in Fig. 4 (a)) from the regression line indicates the chemical production of the chemically active gases. Likewise, an alignment with the regression line indicates the transport-related cause of the chemically active gases. For our analysis, hydrofluoric acid (HF) was chosen as the long-lived trace~~r~~ gas, as it is chemically inert in the stratosphere (Wang et al., 2023).

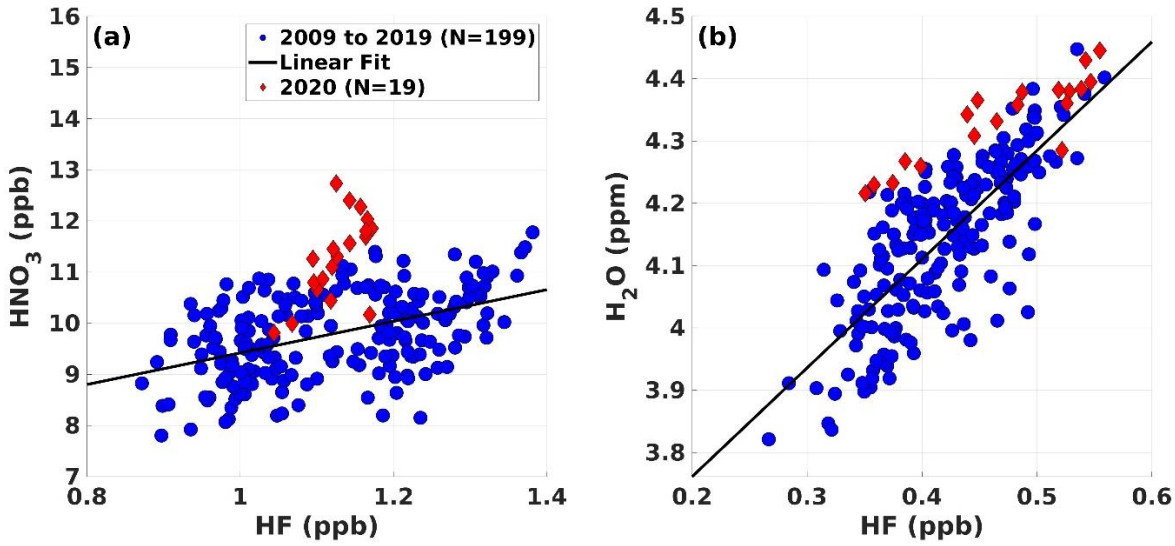


*Figure ~~6~~4: Tracer-~~T~~trace correlation between ACE-FTS (a) $HNO_3$ and HF at the altitude of 25 km, and (b) $H_2O$ vs HF at the altitude of 17 km corresponds to latitude range from -60° to -90°. The blue circles correspond to the period March of 2009–2019, ~~and~~ the red diamonds ~~correspond respectively~~ to the periods ~~March 2009–2019 and~~ March 2020, and the solid black line is a ~~linear fit~~regression line. Here, 'N' is the number of data points used for regression analysis for both subplots.*

The Atmospheric Chemistry Experiment - Fourier Transform Spectrometer (ACE-FTS) obtained HF is regressed against $HNO_3$ and $H_2O$ at altitudes of 25 km and 17 km respectively during March 2009–2019~~2020~~ (Fig. ~~6~~4). The results suggested that the $HNO_3$ was produced through a chemical process as the data corresponding to March 2020 (red diamond in Fig. ~~6~~4a) deviate much from the ~~linear fit~~ regression line (black line). In contrast, increased $H_2O$ is transport-related as the data are close to the ~~linear fit~~ regression line (Fig. ~~6~~4b) and likely carried to the lower stratosphere by the smoke plumes from the black summer event (Schwartz et al., 2020). The production of $HNO_3$ in the lower stratosphere is governed by the heterogeneous chemical reactions in dinitrogen pentoxide ($N_2O_5$) hydrolysis, which can be written as (Zhang et al., 1995):

$$N_2O_5 + H_2O \rightarrow 2HNO_3 \quad \text{(R1)}$$

To confirm the involvement of the $N_2O_5$ hydrolysis process, $H_2O$, $N_2O_5$, and $HNO_3$ from ACE-FTS, and $k_{ext}$ at 745 nm from OMPS at 25 km altitude from February to May 2020 are analyzed and shown in Fig. 5. A coinciding depletion in ACE-FTS $N_2O_5$ at the altitude of 25 km can be observed during the same period (Fig. ~~7a~~5c). Thus, we have ~~and~~ performed a similar tracer-tracer correlation analysis for $N_2O_5$ (Fig. S2). The result indicates that $N_2O_5$ is chemically depleted in the lower stratosphere, suggesting the possible role of the $N_2O_5$ hydrolysis process. In general, the stratospheric background aerosols provide a surface for $H_2O$ to condense and gas-phase $N_2O_5$ reacts with it to form $HNO_3$. ~~To confirm the involvement of the $N_2O_5$ hydrolysis process, $H_2O$, $N_2O_5$, and $HNO_3$ from ACE-FTS, and $k_{ext}$ at 745 nm from OMPS at 25 km altitude from February to May 2020 are analyzed and shown in Fig. 75.~~

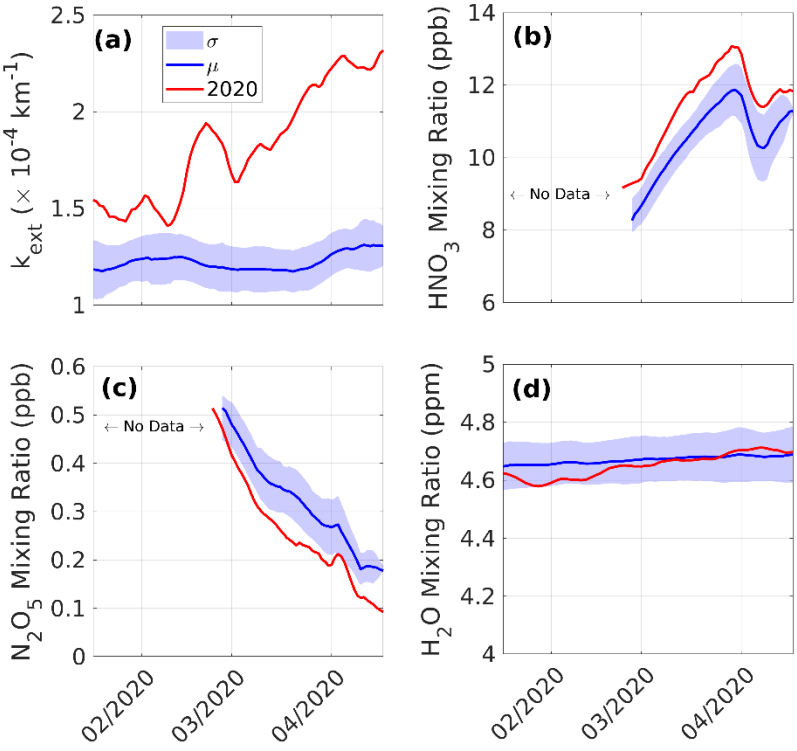


*Figure ~~7~~5: OMPS obtained (a) $k_{ext}$ at 745 nm, and ACE-FTS obtained (b) $HNO_3$, (c) $N_2O_5$, and (d) $H_2O$ mixing ratio at the altitude 25 km averaged between the latitude band -60° to -90°. Here, 'σ' represents the standard deviation with respect to the background mean 'μ' estimated for the period 2009–2019. The x-ticks mark the middle of each month.*

The background mean of $k_{ext}$ remains ~$1.25\times10^{-4}$ $km^{-1}$ between February to May (Fig. ~~7~~5a). But since early 2020, $k_{ext}$ gradually increased to peak at $2.4\times10^{-4}$ $km^{-1}$ by April 2020. This increasing trend of $k_{ext}$ could be attributed to the coupled effect of the transportation of even more bushfire aerosols from mid to high latitude as days passes and aerosol ~~aging~~ ages, ~~where~~ the bushfire aerosols mixed with stratospheric sulfate aerosols result in an increased size and extinction coefficient (Li et al., 2021; Ohneiser et al., 2022). The simultaneous production and depletion of $HNO_3$ and $N_2O_5$ exceeded the respective standard deviations and substantiated that $HNO_3$ is produced through $N_2O_5$ hydrolysis (Fig. ~~7~~5b and c).

During Austral winter, due to the continued lack of solar radiation, the temperature of the polar region decreases ~~by~~ to less than 195 K, which results in the condensation of these trace gases on stratospheric aerosols, forming PSC. The near-simultaneous decrease in aerosol loading (as discussed in Sect. 3.2), $HNO_3$, and $H_2O$ at the lower stratosphere during the early winter of 2020 suggests that these changes possibly affected the PSC formation. A comprehensive investigation of PSC dynamics was carried out using CALIPSO measurements and is discussed in the next section.

### ~~3~~4. Impact of the black summer event on the PSC areal coverage during 2020

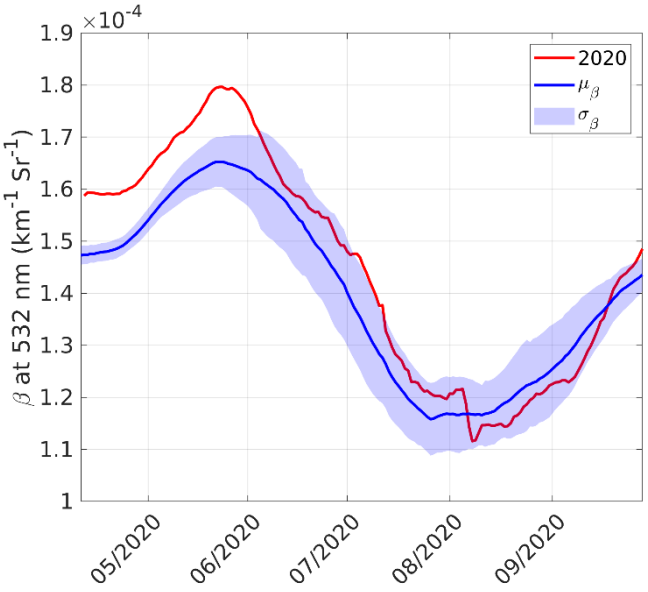


*Figure. 6. Anomaly in CALIPSO observed total attenuated backscatter (β) at 532 nm corresponding to grids classified as 'No Cloud (NC)' at the temperature above $T_{NAT}$. Here, '$\sigma_\beta$' (blue shading region) represents the standard deviation with respect to the background mean '$\mu_\beta$' (solid blue line) estimated for the period 2009–2019. The solid red line corresponds to the 2020 daily mean. The x-ticks mark the middle of each month.*

The total attenuated backscatter (β) at 532 nm measured by CALIPSO for grids classified as 'No Cloud (NC)' at temperatures above the $T_{NAT}$ are chosen to study the influence of the black summer event on lower stratospheric aerosol during the Austral winter 2020 at high latitude region. Since the total attenuated backscatter is above $T_{NAT}$, it could correspond to the lower stratospheric aerosols, thus excluding the influence of sub-visible PSCs or PSCs. From May to mid-June 2020, the total attenuated backscatter varies between $1.6\times10^{-4}$ and $1.8\times10^{-4}$ ($km^{-1}$ $Sr^{-1}$) which is more than one standard deviation with respect to the background mean (Fig. 6). This significant increase in total attenuated backscatter during 2020 is attributed to the intrusion of aerosols from the Black Summer bushfires, which injected a large amount of smoke into the stratosphere, affecting aerosol loading at these altitudes as discussed in previous section.

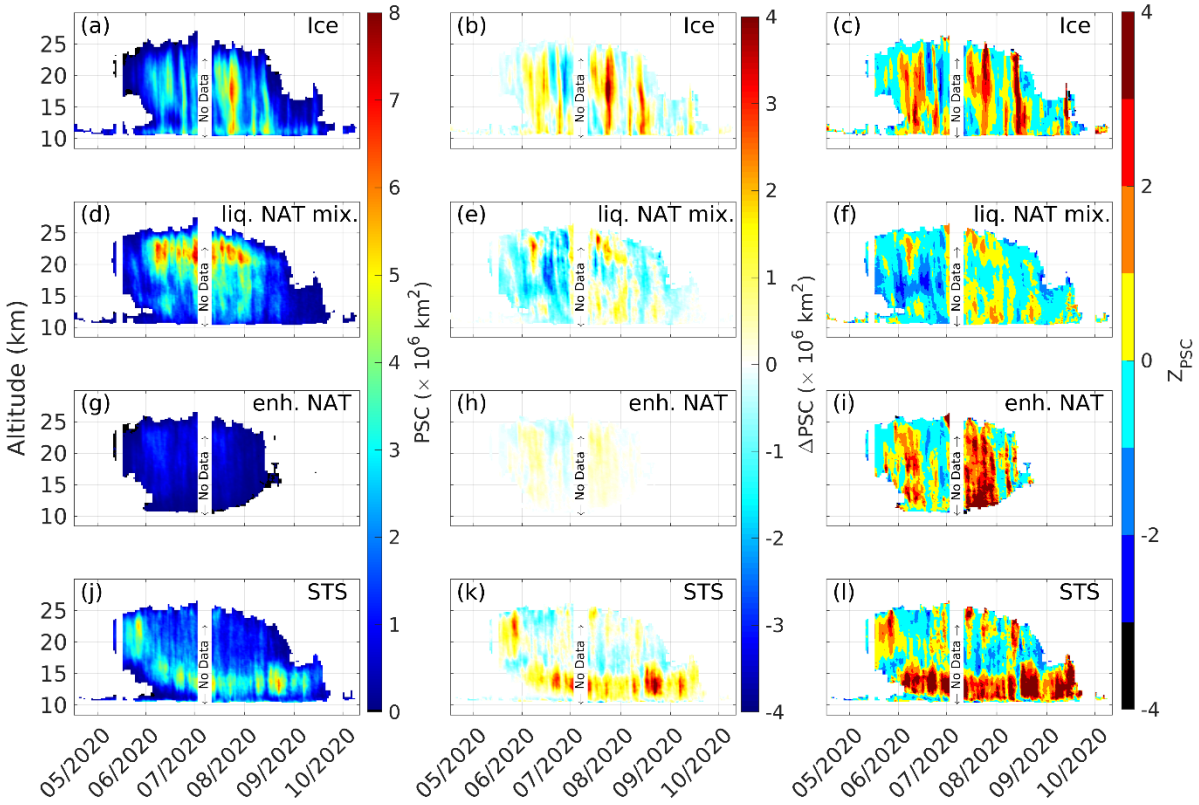


*Figure ~~8~~7: CALIPSO Antarctic PSC monthly mean areal coverage ~~monthly mean~~ (left column, panels a, d, g, and j), anomaly (middle column, panels b, e, h, and k), and standardized anomaly (right column, panels c, f, i, and l) for the year 2020. Here, 'liq. NAT mix.' is a liquid-NAT mixture and enh. NAT is enhanced NAT.*

The Antarctic PSC areal coverage for the year 2020, and corresponding anomalies and standardized anomalies are estimated (as described in the methodology Sect. 2.3) and are shown in Fig. ~~8~~7. CALIPSO detected the PSC from late May onwards (Fig. ~~8~~7) but the depletion in $HNO_3$ has been apparent since mid-April itself (Fig. ~~7c~~5b). This could be due to the sub-visible PSCs whose optical properties are below the detection threshold of the CALIPSO (Lambert et al., 2012; 2016). Peak positive anomaly of up to $4\times10^6$ km$^2$ is exhibited by ice at the altitude between 15 km and 20 km during the second week of August 2020. Followed by ice, the Supercooled Ternary Solution (STS) exhibited a high positive anomaly, which peaked up to $3.5\times10^6$ km$^2$ at an altitude between 12 km and 15 km during early September 2020. ~~Since the STS is always in the liquid state and has a relatively higher surface area density than the solid PSCs, the amplification in the STS areal coverage can potentially promote the heterogeneous chlorine activation reaction and lead to additional ozone loss~~ (Molina et al., 1993; Carslaw et al., 1994; Ravishankara and Hanson, 1996)~~.~~ Similarly, an increase in enhanced NAT~~Enhanced Nitric Acid Trihydrate (ENAT)~~ areal coverage is observed but its contribution to the total PSC areal coverage is negligible. It is evident from Fig. ~~8~~7 (b, h, and k) that the positive anomalies in the areal coverage of PSCs like ice, STS, and ~~ENAT~~ enhanced NAT exceeded three standard deviations with respect to the background mean. The increase in $HNO_3$ containing PSCs: STS and ~~ENAT~~ enhanced NAT can be attributed to the increased surface area provided by the bushfire aerosols and the production of $HNO_3$ through the $N_2O_5$ hydrolysis process. In contrast, the areal coverage of another $HNO_3$ containing PSC, i.e., liquid−NAT mixtures~~Liquid Nitric Acid Trihydrate (LNAT)~~, exhibited strong negative anomalies (Fig. ~~8~~7 (e and~~,~~ f)).

For instance, during June and July 2020, areal coverage of liquid−NAT mixtures~~LNAT~~ decreased significantly, leading to a negative anomaly of up to $2.5\times10^6$ km$^2$, which is more than two standard deviations from the background mean (Fig. ~~8~~7 (e and~~,~~ f)). During the same period, a significant increase in ice areal coverage of up to $2\times10^6$ km$^2$ is observed, exceeding two standard deviations (Fig. ~~8~~7 (b and~~,~~ c)). Similar simultaneous positive and negative anomalies in ice and liquid−NAT mixtures~~LNAT~~ are observed during August 2020 as well. As NAT can serve as efficient nuclei for ice formation (Hoyle et al., 2013), this anomaly could be due to the heterogeneous nucleation process of ice on existing NAT PSC. To verify this hypothesis, we performed Lagrangian backward trajectory analysis of the ice PSC as well as liquid-NAT mixture PSC to study their respective formation pathways as discussed in the methodology section (Sect. 3.3)~~we developed a novel methodology which retrieves the PSC formation pathways~~, and the results are discussed in the next section.

### ~~3~~4.5. Formation pathways of liquid–NAT mixture ~~LNAT~~ and ~~I~~ice PSC

In this section, the formation pathways of ice and liquid-NAT mixture PSCs are presented in the form of case studies. A total of 6 case studies are discussed: 4 cases for liquid-NAT mixture PSC and 2 cases for ice PSC. The liquid-NAT mixture and ice PSCs are selected according to the selection criteria discussed in Sect 3.3 and backward trajectories are calculated using the CLaMS trajectory module with meteorological parameters obtained from the ERA5 operational analysis dataset. The liquid-NAT mixture can form either through an ice-free nucleation process or an ice–assisted nucleation process. The evidence of the former one is discussed through case no. 1 to 2 and the latter one is discussed through case no. 3 to 4 below. Similarly, the evidence of the formation of ice without NAT and with NAT are discussed through case no. 5 and 6 respectively.

#### 4.5.1 Ice-free nucleation of liquid-NAT mixture PSC

~~The PSC formation pathways are retrieved from the CALIPSO PSC measurements, as described in Sect. 2.3, during the Austral winter of 2020, and are shown in Fig. 9.~~

In this section, we discuss two cases: case no. 1 where ‘NC’ precedes the liquid-NAT mixture along the trajectory, and case no. 2 where STS precedes the liquid-NAT mixture. In both cases, there is no evidence of the formation of ice either through CALIPSO observation or conditions conducive for ice formation, suggesting the possibility of ice-free nucleation of liquid-NAT mixture.

Case no. 1: NC precedes liquid-NAT mixture

On 10-07-2020, at 18:00 UTC, CALIPSO detected a liquid-NAT mixture at a latitude of -69.1° and longitude of 99.15°, with a potential temperature of 484 K. This observation is marked by a yellow diamond in Fig. 8(a) and corresponding CALIPSO scan track is shown as a solid grey line. The dashed black line in Fig. 8(a) represents the calculated 48 h backward trajectory of this PSC, with the color indicating the temperature history of the air parcel in $_{ice}$ coordinates (i.e. ambient temperature - the frost point ($T_{ice}$)). The temperature ‘T’ is obtained from ERA5 operational analysis, and $T_{ice}$ is estimated using the ERA5 pressure, and mean MLS $H_2O$ mixing ratio found along the trajectory following Marti and Mauersberger, (1993).

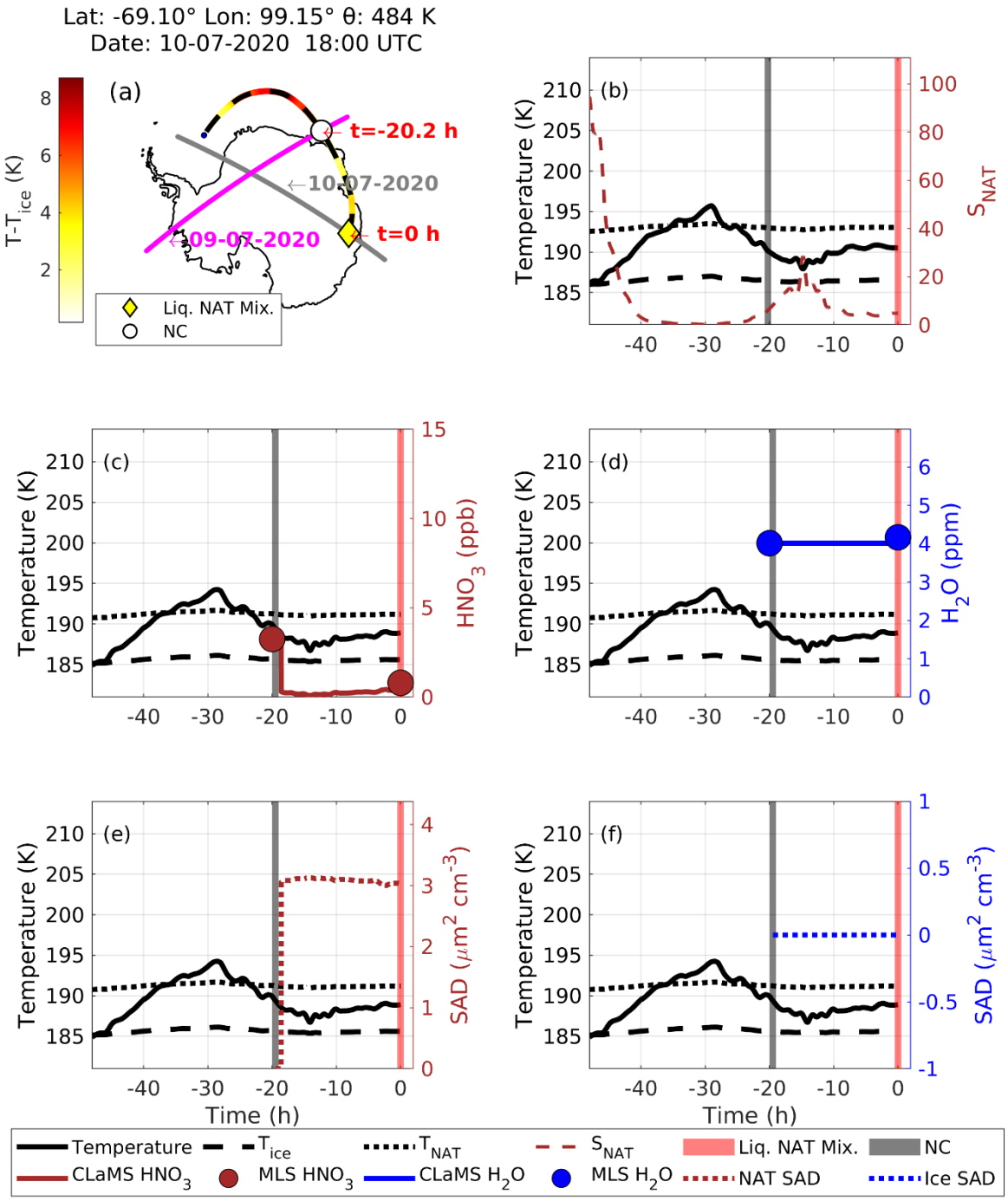


Figure 8. (a) The Lagrangian backward trajectory for a 48 h period starting at time, t = 0 h (corresponding to 18:00 UTC 10-07-2020). Here, the dashed black line is the backward trajectory and the color along this trajectory is the temperature at the T-$T_{ice}$ coordinate. The yellow diamond represents the observed liquid-NAT mixture from the CALIPSO scan track (solid grey line) corresponding to 10-07-2020. The complete coordinate of this liquid-NAT mixture is given in the title. The white circle represents the observed 'No Cloud (NC)' at the time, t = -20.2 h from the CALIPSO scan track (solid magenta line) corresponding to 09-07-2020. (b) the saturation ratio over

NAT ($S_{NAT}$) (dashed brown line) and vertical bars mark the liquid-NAT mixture (red) and 'NC' (grey). (c) The brown circle marks the MLS $HNO_3$, and the solid brown line represents the CLaMS $HNO_3$. (d) The blue circle marks the MLS $H_2O$, and the solid blue line represents the CLaMS $H_2O$. (e) the NAT surface area density (SAD) (dotted brown line), (f) The ice surface area density (SAD) (dotted blue line).

The backward trajectory revealed that CALIPSO observed 'No Cloud (NC)' along this trajectory 20.2 hours earlier (at the time, t = -20.2 h), on 09-07-2020, marked by a white circle in Fig. 8(a). The temperature history shows that between these two observations, the temperature did not decrease below the $T_{ice}$, indicating that the condition is not conducive for ice formation. At the time of the NC observation, the temperature is ~189 K which is 2 K below the NAT temperature ($T_{NAT}$). During this time, MLS observed gas-phase $HNO_3$ and $H_2O$ mixing ratios are 3.5 ppb and 4 ppm, respectively (Fig. 8 (c) and (d)). Using these as initial conditions, a CLaMS box model run was performed from t = -20.2 h to 0 h, simulating the evolution from the NC to the liquid-NAT mixture. After 20.2 hours, the MLS $HNO_3$ decreased from 3.5 to 0.5 ppb, with no significant change in MLS $H_2O$. Figure 8(c) and (d) show that the CLaMS modeled uptake of $HNO_3$ and $H_2O$ which agrees well with the MLS observations. Furthermore, the CLaMS box model run indicates that the NAT surface area density (SAD) increased to nearly 3 $\mu m^2\ cm^{-3}$ (shown in Fig. 8(e)), while the ice SAD remained at 0 $\mu m^2\ cm^{-3}$, confirming that no ice formation occurred before the observation of the liquid-NAT mixture. During the transition from 'No Cloud' (NC) to the liquid-NAT mixture, the saturation ratio over NAT stayed well below 30, further supporting the absence of ice involvement in the formation of the liquid-NAT mixture (Fig. 8(b)) (Luo et al., 2003; Voigt et al., 2005). Since the liquid-NAT mixture represents the mixture of liquid STS and solid NAT, it should be noted that STS PSC should have formed between this transition and specifically before the formation of NAT.

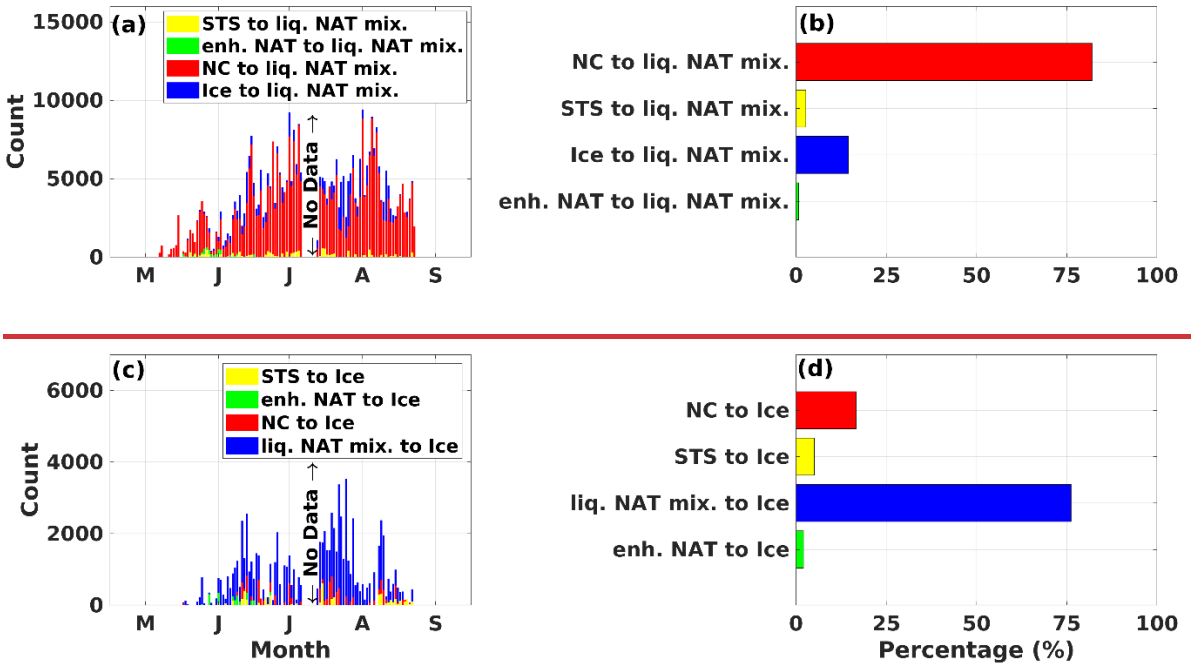


*Figure 9: (a) Formation pathways of LNAT, (b) percentage contribution of LNAT formation pathways, (c)*

~~*Formation pathways of ice, and (d) percentage contribution of ice formation pathways, for the year 2020. The 'Count' in the y-axis of panels (a) and (c) represents the number of CALIPSO grids or pixels exhibiting transition in PSC composition. The x-ticks mark the middle of each month.*~~

Case no. 2: STS precedes liquid-NAT mixture

In case no. 2, STS is found to appear along the backward trajectory before the appearance of the liquid-NAT mixture. On 10-08-2020, at 03:00 UTC, CALIPSO detected a liquid-NAT mixture at a latitude of -67.1° and longitude of 325.57°, with a potential temperature of 409 K. This observation is marked by a yellow diamond in Fig. 9 (a) and corresponds to the CALIPSO scan track shown as a solid grey line. The dashed black line in Fig. 9 (a) represents the calculated 48 h backward trajectory of this PSC, with the color indicating the temperature history of the air parcel in $T\text{-}T_{ice}$ coordinates as discussed in case no. 1.

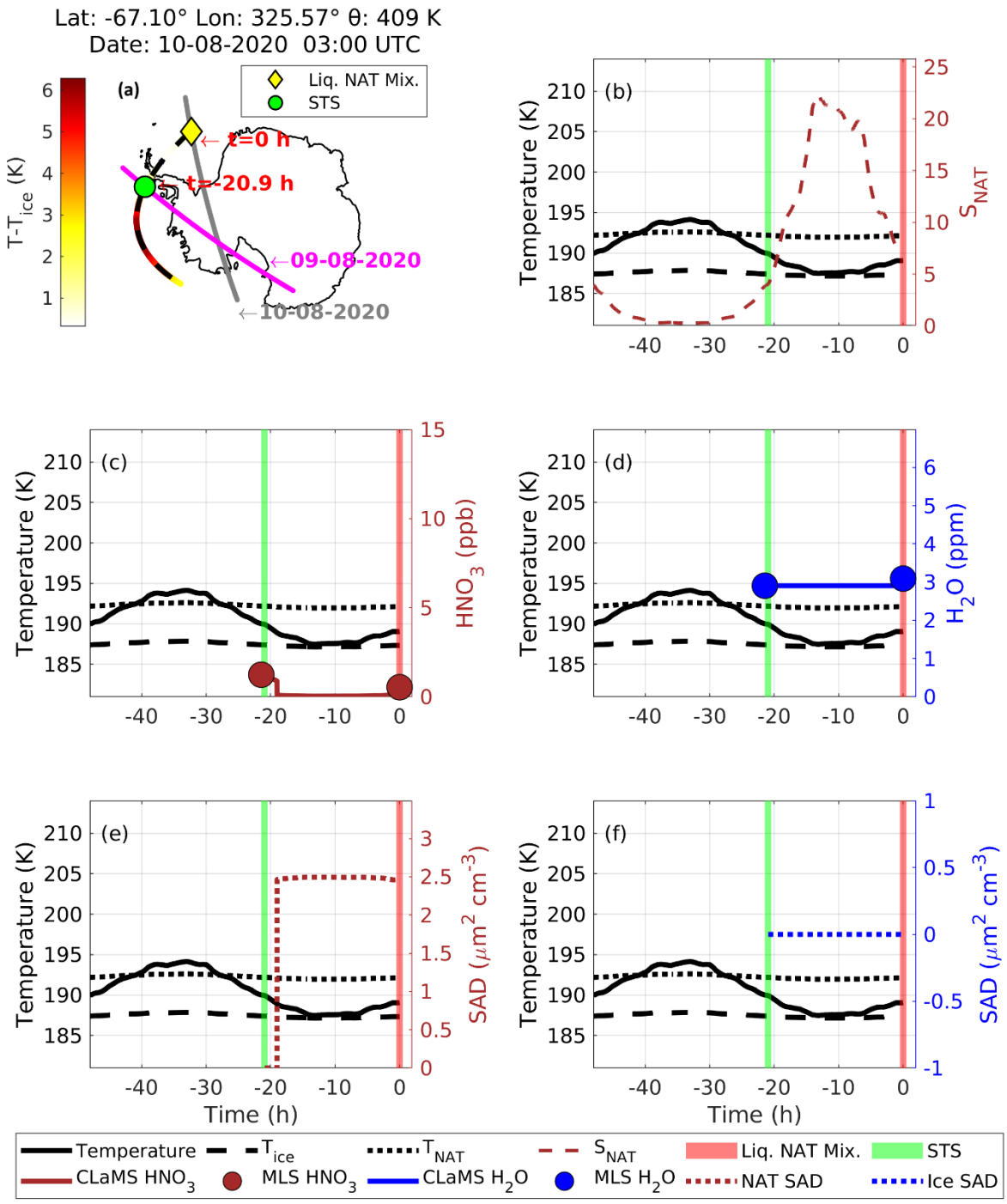


Figure 9. Same as Fig. 8 but for Case no. 2 where STS preceded the liquid-NAT mixture along the Lagrangian backward trajectory.

The backward trajectory indicated that CALIPSO detected STS along this path 20.9 hours prior (at the time, t = -20.9 h), on 09-08-2020, marked by a green circle in Fig. 9 (a). The temperature history shows that between these two observations, the temperature did not decrease below $T_{ice}$, similar to Case no. 1, which again suggests that ice formation was unlikely to occur. At the time of the STS detection, the temperature was approximately 190 K, which is 3 K below $T_{NAT}$. During this period, MLS observed gas-phase $HNO_3$ and $H_2O$ mixing ratios of 1.7 ppb and 3 ppm, respectively. During the transition of STS to liquid-NAT mixture from t = -20.9 h to 0 h, the MLS

$HNO_3$ dropped from 1.7 to 0.3 ppb, with no notable change in MLS $H_2O$. The CLaMS modeled uptake of $HNO_3$, and $H_2O$ aligned well with the MLS observations (Fig. 9 (c) and (d)). Additionally, the CLaMS box model simulation shows that the NAT SAD increased to nearly 2.5 $\mu m^2\ cm^{-3}$ (Fig. 9 (e)), while the ice SAD remained at 0 $\mu m^2\ cm^{-3}$, confirming that no ice formed before the observation of the liquid-NAT mixture in case no. 2 as well. During the transition from STS to the liquid-NAT mixture, the $S_{NAT}$ remained well below 25, further substantiating the absence of ice involvement in the formation of the liquid-NAT mixture (Fig. 9 (b)).

In these two cases of ice-free nucleation of liquid-NAT mixture discussed above, the temperature of these trajectories has not decreased below $T_{ice}$, and $S_{NAT}$ has remained below 30, confirming no involvement of ice during liquid-NAT mixture formation.

**4.5.2 Ice-assisted nucleation of liquid-NAT mixture PSC**

Here, two cases are discussed through case no.3 and case no.4. In the former case, the direct CALIPSO observation of ice preceding the liquid-NAT mixture along the trajectory is presented. In the latter case, CALIPSO observed 'NC' preceding the liquid-NAT mixture, but the conducive conditions for ice formation are found before the formation of the liquid-NAT mixture, indicating the possibility of an ice–assisted nucleation process.

Case no. 3: Ice precedes liquid-NAT mixture

In this case, ice has appeared along the backward trajectory before the appearance of the liquid-NAT mixture, indicating nucleation of NAT on the pre-existing ice PSC. On 05-07-2020, at 23:00 UTC, CALIPSO detected a liquid-NAT mixture (yellow diamond in Fig. 10 (a)) at a latitude of -66.89° and longitude of 25.89°, with a potential temperature of 510 K. Before this, CALIPSO observed ice PSC along this trajectory at time, t = -43 h during 04-07-2020 (blue star in Fig. 10 (a)).

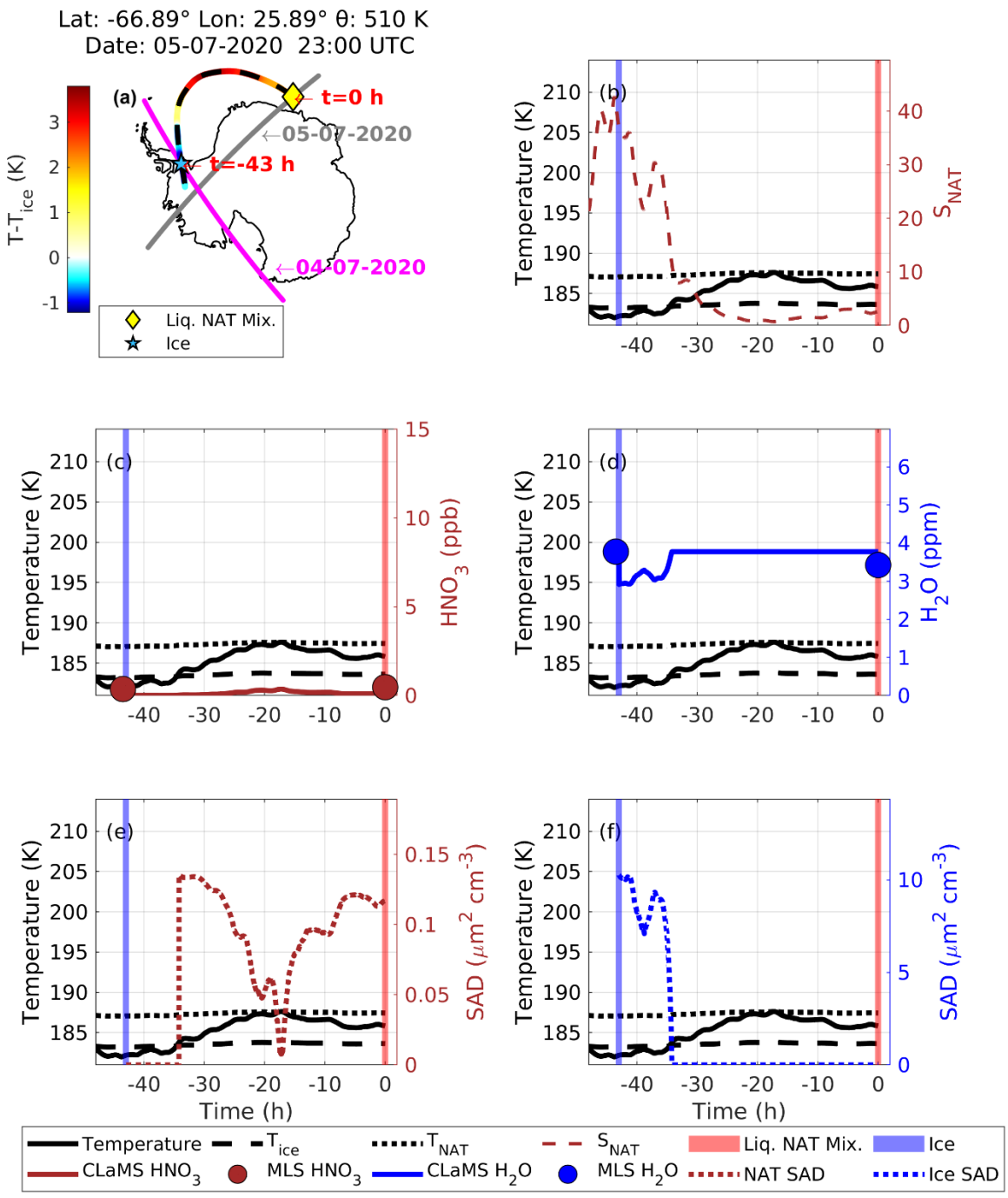


Figure 10. Similar to Fig. 8 but for the Case no. 3 where ice preceded the liquid-NAT mixture along the Lagrangian backward trajectory.

At the time of the ice detection, the temperature was approximately 181.5 K, which is 1.5 K below $T_{ice}$. During this time, MLS observed gas-phase $HNO_3$ and $H_2O$ mixing ratios are 0.37 ppb and 3.9 ppm, respectively. Furthermore, at this time, according to the CLaMS box model run, ice SAD is ~ 10 $\mu m^2$ $cm^{-3}$ and NAT SAD is 0 $\mu m^2$ $cm^{-3}$ (Fig. 10 (e) and (f)). After this, the temperature gradually increases, exceeding $T_{ice}$ which makes ice SAD to 0 $\mu m^2$ $cm^{-3}$, and NAT SAD peaks to 0.14 $\mu m^2$ $cm^{-3}$ which is possibly due to nucleation of NAT particles on this ice. During the transition from ice to the liquid-NAT mixture, the maximum $S_{NAT}$ is observed to be 43 at

the time, t = -43 h. The MLS observed $HNO_3$ changed from 0.37 ppb to 0.47 ppb whereas, $H_2O$ decreased from 3.7 ppb to 3.4 ppb. It should be noted that these changes in $HNO_3$ and $H_2O$ are within MLS measurement uncertainty.

Case no. 4: NC precedes liquid-NAT mixture

In this case, NC is observed before the observation of the liquid-NAT mixture. But along the trajectory, the temperature decreased well below ice formation temperature (i.e., below $T_{ice}$-1.5 K), indicating the possible formation of ice and thus nucleation of NAT on this ice PSC.

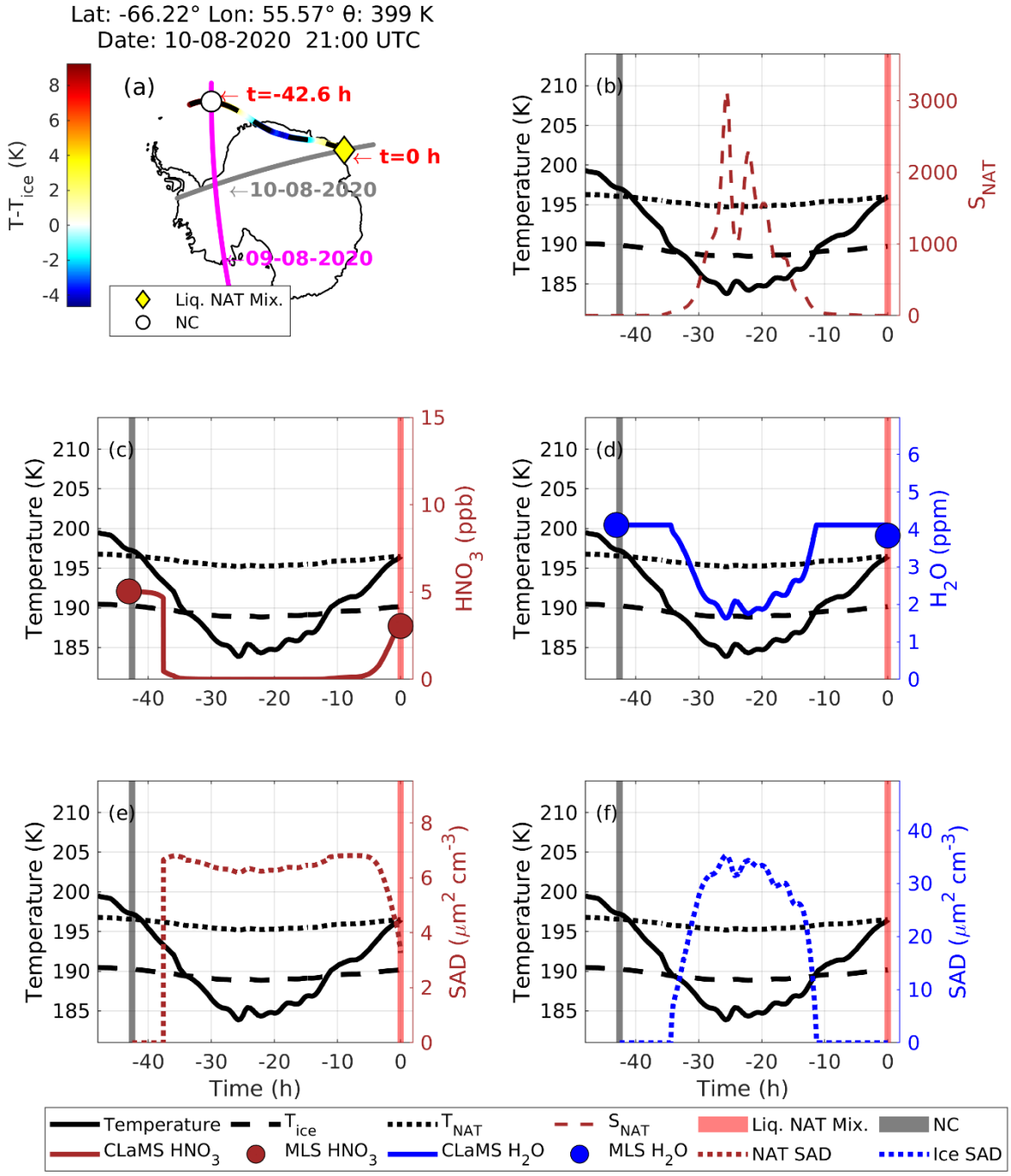

Figure 11. Similar to Fig. 8 but for Case no. 4 where NC preceded the liquid-NAT mixture along the Lagrangian backward trajectory.

On 10-08-2020, at 21:00 UTC, CALIPSO detected a liquid-NAT mixture (indicated by a yellow diamond in Fig. 11(a)) at a latitude of -66.22° and longitude of 55.57°, with a potential temperature of 399 K. Before this observation, CALIPSO observed 'No Cloud' (NC) along this trajectory at time t = -42.6 h on 09-08-2020. During that period, the temperature was around 197 K, which is 0.4 K above the $T_{NAT}$, and MLS measured gas-phase $HNO_3$ and $H_2O$ mixing ratios of 5 ppb and 4.1 ppm, respectively. These conditions were not favorable for the formation of any type of PSCs. Approximately 4.6 hours later (i.e., at time t = -38 h), the temperature decreased below $T_{NAT}$ by 3 K, which likely promoted the formation of NAT, as supported by the CLaMS box model run, with NAT SAD reaching up to 6 $\mu m^2\ cm^{-3}$ (Fig. 11(e)). No ice formation occurred at this stage, as the temperature remained above $T_{ice}$. The temperature continued to decline, reaching $T_{ice}$ at time t = -35 h, at which point ice began to appear in the CLaMS model, as indicated by the ice SAD (Fig. 11(f)).

As the temperature fell to 184 K, which is 5 K below $T_{ice}$, the ice SAD peaked at 35 $\mu m^2\ cm^{-3}$, suggesting that these ice particles may have nucleated on the previously formed NAT. By this time, the CLaMS model shows that $HNO_3$ had nearly depleted from the initial 5 ppb to 0.002 ppb, while $H_2O$ decreased from 4.1 ppm to 1.6 ppm. Additionally, $S_{NAT}$ peaked at ~ 3000 (Fig. 11 (b)). Unlike in cases 1 and 2, where ice was not involved in NAT formation, a significant change in $H_2O$ was observed in this instance due to the formation of ice. Subsequently, the temperature began to increase gradually, reaching above $T_{ice}$ at time t = -11 h, resulting in an ice SAD of 0 $\mu m^2\ cm^{-3}$. At this point, all condensed $H_2O$ evaporated back into the gas phase, returning to the initial level of 4.1 ppm. In contrast, the gas-phase $HNO_3$ remained below 0.1 ppb. The temperature continued to increase, and at the time, t = 0 h, CALIPSO detected a liquid-NAT mixture, during which MLS observed $HNO_3$ levels at 3.1 ppb, while the CLaMS modeled $HNO_3$ is at 3.5 ppb. Throughout this process, MLS $HNO_3$ decreased from 5 ppb to 3.1 ppb, leaving 1.9 ppb in the condensed phase. In summary, when the temperature was above $T_{NAT}$, no cloud was observed by CALIPSO. As the temperature decreased below $T_{NAT}$ - 3 K, NAT formed first, followed by ice nucleation when the temperature decreased further below $T_{ice}$. As the temperature increased, additional NAT particles nucleated on the existing ice. Though the CLaMS box model suggests the presence of ice between t = -35 h to -11 h, there were no co-located CALIPSO observations along the trajectory to verify the presence of ice PSC. However, we identified another backward trajectory related to the CALIPSO-detected liquid-NAT mixture at a potential temperature of 388 K (which is 11 K lower than the current trajectory of 399 K), as shown in Fig. S3. The temperature fluctuations along this trajectory are similar to those in case no. 4, where a co-located CALIPSO observation of ice PSC was recorded at time t = -29.4 h. A similar case, where STS precedes the liquid-NAT mixture, but the temperature along the trajectory decreased below the $T_{ice}$, creating conditions favorable for ice formation along with the CLaMS box model run, is presented in Fig. S4. Given the similarities between this case and case no. 4, which has been described above, we have not provided a detailed analysis of the case where STS precedes the liquid-NAT mixture.

In these two cases of ice–assisted nucleation process of liquid-NAT mixture, the temperature decreased below $T_{ice,}$ and $S_{NAT}$ increased more than 30. Therefore, the extent to which the temperature decreased below $T_{ice}$ and the extent to which the $S_{NAT}$ increased along the trajectories from the instant of observation of NC/STS/ice to the

instant of observation of the liquid-NAT mixture can act as proxies to determine whether the liquid-NAT mixture is formed via ice–assisted or ice-free nucleation process.

### 4.5.3 Validation of uptakes of $HNO_3$ and $H_2O$ observed during liquid-NAT mixture formation

During the formation of the liquid-NAT mixture, changes in the gas phase concentrations of MLS $HNO_3$ and $H_2O$ were observed, as previously discussed. We used the CLaMS microphysical box model to simulate the formation of the liquid-NAT mixture based on the backward trajectories and modeled the uptakes of $HNO_3$ and $H_2O$. These results were validated against the observed uptakes from MLS, as shown in Fig. 12. This result includes both the ice–assisted and ice-free nucleation of the liquid-NAT mixture.

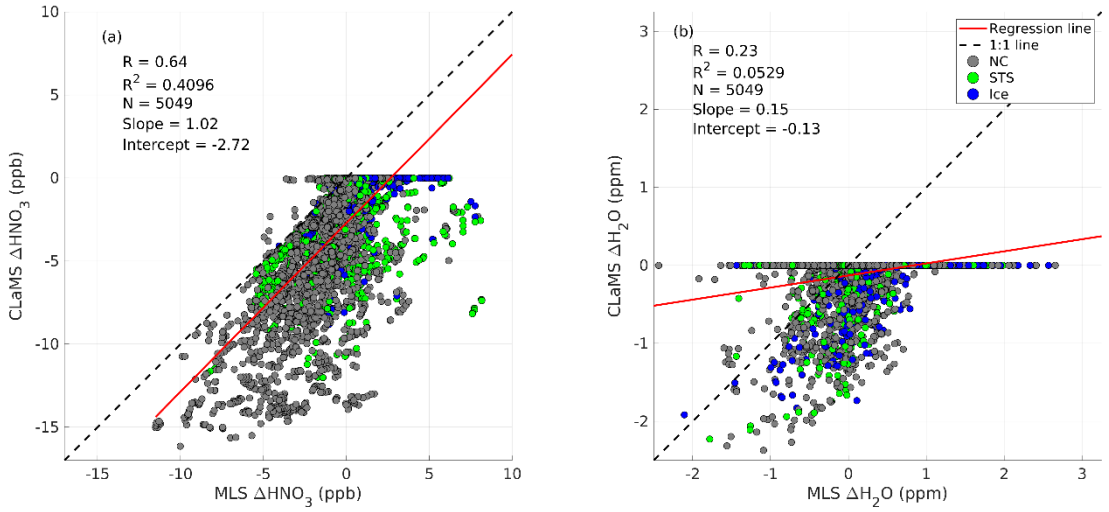


Figure 12. (a) shows a scatter plot of MLS observed change (Δ) in $HNO_3$ (ppb) against the CLaMS modeled change in $HNO_3$ (ppb), (b) shows a scatter plot of MLS observed change (Δ) in $H_2O$ (ppm) against the CLaMS modeled change in $H_2O$ (ppm). The dashed line represents a 1:1 fit, and the solid red line represents the linear regression line. Here, 'R' is the correlation coefficient, '$R^2$' is the correlation of determination, and N is the total number of data points used. The color of the circles corresponds to each PSC type preceding to liquid-NAT mixture along the backward trajectory. Grey for NC, green for STS, and blue for ice PSC.

A strong correlation is found between the MLS observed change in $HNO_3$ ($\Delta HNO_3$) and the CLaMS modeled change in $HNO_3$, with a correlation coefficient (R) of 0.64 and a coefficient of determination ($R^2$) of 0.4096 (Fig. 12(a)). The intercept of -2.72 suggests that the CLaMS model overestimates the $HNO_3$ condensation during NAT formation. It could be due to bias in temperature from ERA5 operational analysis which is used in this paper. The ERA5 operational analysis temperature is consistently 1 K lower than the radiosonde-measured temperature (Engel et al., 2013). Due to this cold bias, the CLaMS model overestimates the condensation of $HNO_3$, leading to the negative value of intercept. Furthermore, significant $HNO_3$ uptake of up to 12 ppb, as observed by MLS, occurs when NC preceded the observation of the liquid-NAT mixture along the trajectory (indicated by the grey circle in Fig. 12(a)). However, a relatively low $HNO_3$ uptake is observed for cases where STS preceded the liquid-

NAT mixture (marked by the green circle in Fig. 12(a)). It is important to note that ice may have formed during the transition from NC/STS to the liquid-NAT mixture, as discussed in case no. 4. Furthermore, in most cases where ice preceded the liquid-NAT mixture along the trajectory, a positive change in MLS $\Delta HNO_3$ is observed and more detailed studies are required to understand the physical mechanism behind it.

In the case of $H_2O$ uptake, a weak correlation is found between MLS $\Delta H_2O$ and CLaMS $\Delta H_2O$, with a correlation coefficient (R) of 0.23 and a coefficient of determination ($R^2$) of 0.0529 (Fig. 12(b)). In addition to the cold temperature bias in ERA5 operational analysis, this low correlation is also attributed to the fact that in the CLaMS model, the initialized $H_2O$ at the beginning of the trajectory changes only if ice forms during the liquid-NAT mixture formation, resulting in most of the CLaMS $\Delta H_2O$ values remaining at zero. However, there are a few instances where changes in $H_2O$ are observed in both CLaMS and MLS, potentially indicating ice–assisted formation of the liquid-NAT mixture.

### 4.5.4 Relative percentage contribution of liquid-NAT mixture formation pathway

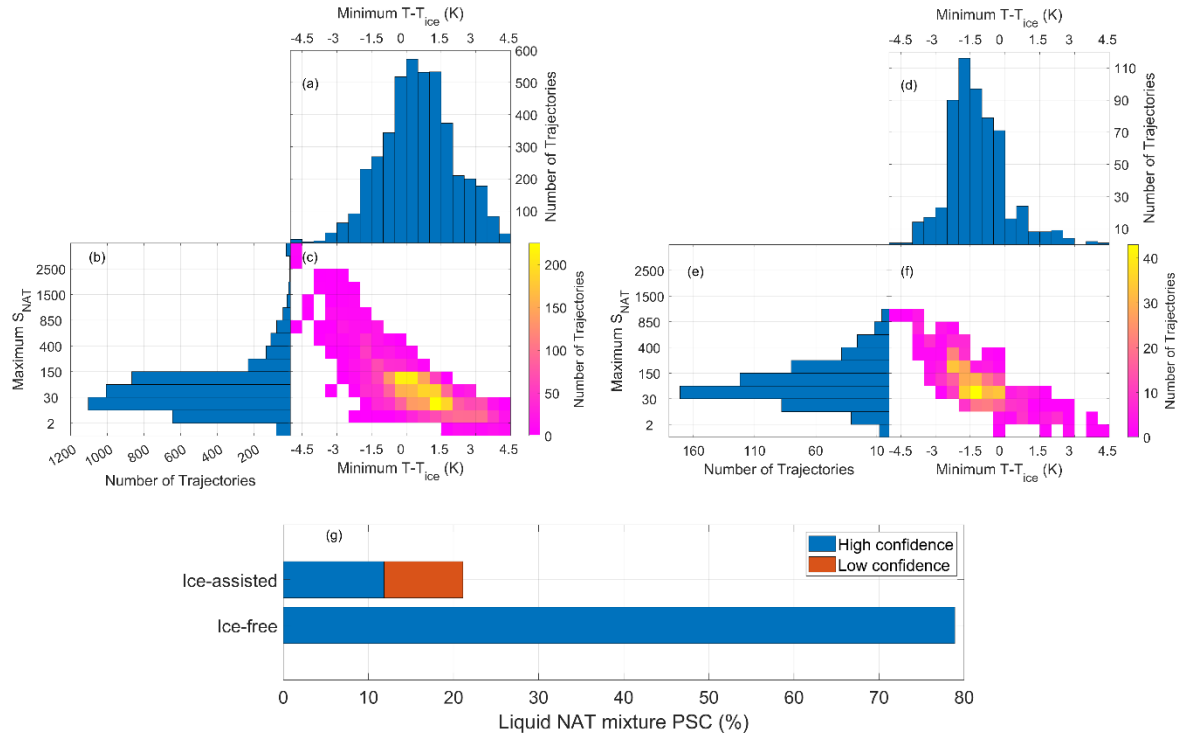


Figure. 13. Histograms and joint histograms of the minimum T - $T_{ice}$ and the maximum $S_{NAT}$ (saturation ratio over NAT) along the trajectories are shown. Panels (a–c) correspond to the backward trajectories where NC/STS preceded the liquid-NAT mixture CALIPSO observation. Panels (d–f) are similar to (a–c) but for the case of ice preceding liquid-NAT mixture. Panel (g) shows the percentage of liquid NAT mixture formed through ice–assisted and ice-free nucleation processes.

As discussed in case studies 1 and 2, the presence of NC/STS preceding the liquid-NAT mixture along the trajectories does not exclude the involvement of ice in the formation of the liquid-NAT mixture. It is possible that ice could have formed before the observation of the liquid-NAT mixture if the temperature decreased below $T_{ice}$

and reached a state of high NAT supersaturation. Therefore, the extent of temperature decrease below $T_{ice}$ and the corresponding increase in $S_{NAT}$ along the trajectories, from the time of NC/STS observation to the formation of the liquid-NAT mixture, can serve as indicators for whether the liquid-NAT mixture formed through ice–assisted or ice-free nucleation. To investigate this, we created two sets of histograms. Figure. 13(a–c) shows the histograms of minimum T-$T_{ice}$ and maximum $S_{NAT}$ along the trajectories for cases where NC/STS preceded the liquid-NAT mixture. Figure 13(d–f) shows similar histograms for cases where ice preceded the liquid-NAT mixture. In all cases, the minimum T-$T_{ice}$ and maximum $S_{NAT}$ were considered only from the time of NC/STS (for Fig. 13 (a-c)) or ice (for Fig. 13(d-f)) observation until the liquid-NAT mixture formed.

For cases where NC/STS preceded the liquid-NAT mixture, the histogram of minimum T-$T_{ice}$ (Fig. 13(a)) shows that most trajectories experienced T-$T_{ice}$ values between -0.5 K and 1.5 K, with the highest peak between 0 and 0.5 K. Similarly, the histogram of maximum $S_{NAT}$ (Fig. 13(b)) shows that most trajectories had $S_{NAT}$ values ranging from 15 to 150, with a peak between 15 and 30. A cluster of trajectories (represented by yellow to orange grids) is visible in the joint histogram (Fig. 13(c)) within this range. For the formation of ice along these trajectories, the temperature should have reached at least -1.5 K for heterogeneous nucleation of ice, and a high $S_{NAT}$ of > 500 (Luo et al., 2003) should have occurred for nucleation of NAT on these ice particles. Since neither of these is observed and conditions are not conducive to ice formation, it is highly likely that the liquid-NAT mixture formed through an ice-free nucleation process. Case no. 1 and case no. 2, which were discussed earlier belong to this category.

In addition, when the minimum T-$T_{ice}$ decreased below -1.5 K, the air parcels reached high supersaturation, with $S_{NAT}$ values exceedingly even 500. Case no. 4 which was discussed earlier belongs to this category. Under these conditions, the formation of ice and subsequent nucleation of NAT on this ice is likely, indicating that the liquid-NAT mixture may have formed through ice–assisted nucleation. This observation aligns with previous findings by (Luo et al., (2003) on NAT formation over ice under high supersaturation conditions.

For cases where ice preceded the liquid-NAT mixture along the trajectory, the histogram of minimum T-$T_{ice}$ (Fig. 13(d)) shows that most trajectories experienced T-$T_{ice}$ values between -2 K and -1 K, with the highest peak between -2 K and -1.5 K. Similarly, the histogram of maximum $S_{NAT}$ (Fig. 13(e)) shows that most trajectories had $S_{NAT}$ values ranging from 15 to 150, but for this case, the highest peak occurs between 30-70 instead of 15-30 in previous case. A cluster of trajectories (represented by yellow to orange grids) is visible in the joint histogram (Fig. 13(f)) within this range. Case no. 3 which was discussed earlier belongs to this category where ice preceded the liquid-NAT mixture.

From these two sets of histograms, an apparent shift in minimum T-$T_{ice}$ is evident between cases where NC/STS preceded the liquid-NAT mixture (peak between 0 and 0.5 K) and cases where ice preceded the liquid-NAT mixture (peak between -2 and -1.5 K). In contrast, only a subtle shift is observed in maximum $S_{NAT}$. Therefore, to determine whether ice was involved in the formation of the liquid-NAT mixture, we primarily rely on the minimum T-$T_{ice}$ reached by each trajectory, rather than the maximum $S_{NAT}$.

For the cases where ice preceded liquid-NAT mixture, we classified these as ice–assisted nucleation of liquid-NAT mixture with high confidence. This is classified with 'high confidence', because we have CALIPSO observation of the presence of ice along the trajectory similar to case no. 3. And, for the cases where NC/STS preceded the liquid-NAT mixture if the temperature along the trajectories decreased less than -1.5 K, we included it to the ice–assisted nucleation of liquid-NAT mixture with low confidence. These are classified with low confidence because ice formation is not directly observed by CALIPSO but possibly formed as the temperature decreased 1.5 K below $T_{ice}$. For the cases where NC/STS preceded the liquid-NAT mixture if the temperature along the trajectories has not decreased less than -1.5 K, we classified them as ice-free nucleation of liquid-NAT mixture with high confidence. The final retrieved relative percentage of the liquid-NAT mixture formation pathway is shown in Fig. 13 (g). It shows that 79 % of the liquid-NAT mixture is formed through an ice-free formation process with high confidence. Almost 12 % and 9 % of the liquid-NAT mixture formed through an ice–assisted formation process with high and low confidence respectively.

#### 4.5.6 NAT-assisted ice formation

Case 5: Liquid-NAT mixture precedes ice PSC

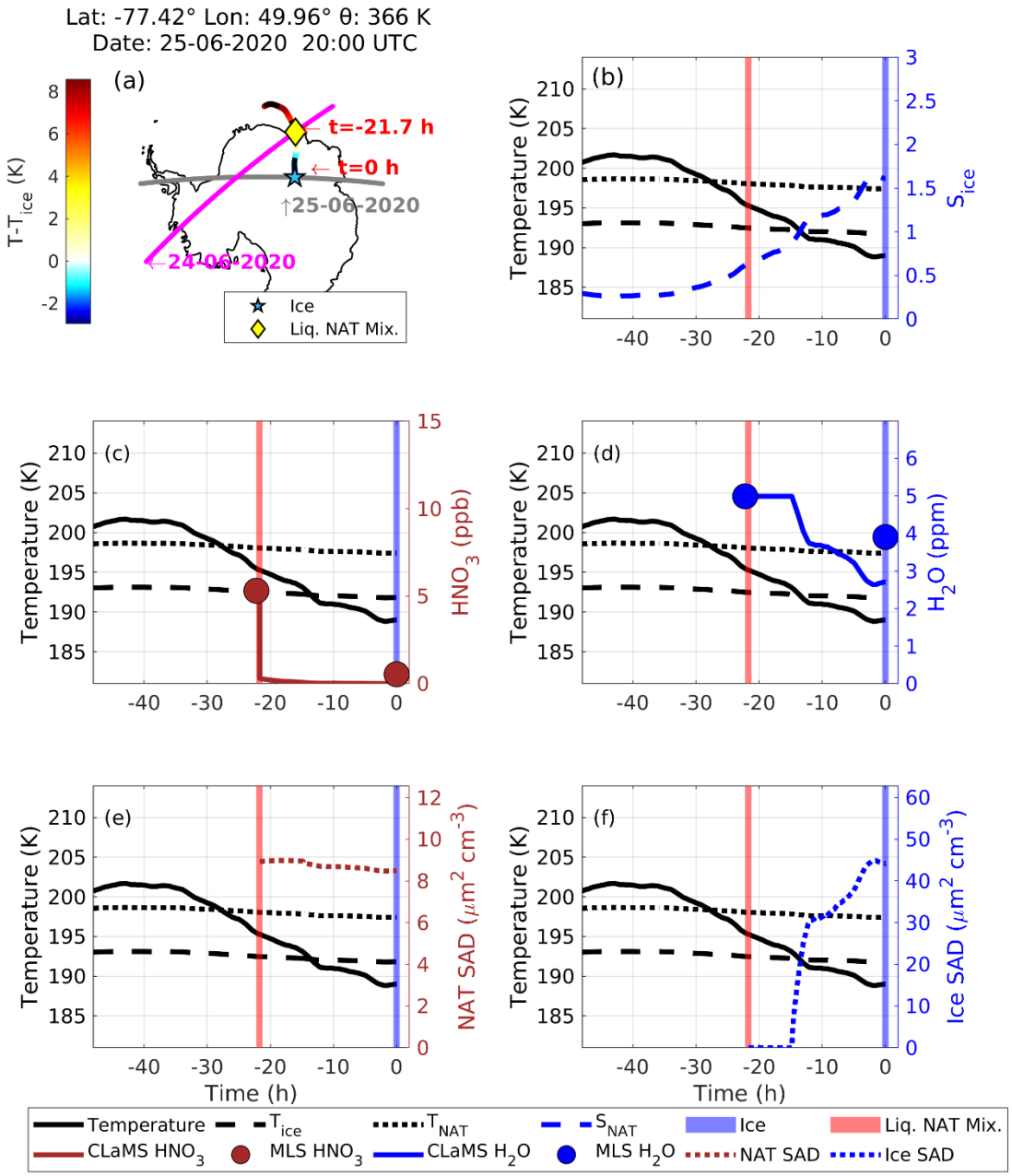


Figure 14. Same as Fig. 8 but for case no. 5 where ice nucleation on NAT is shown.

In this case, the liquid-NAT mixture is observed before the observation of ice, indicating nucleation of ice on the liquid-NAT mixture. On 25-06-2020, at 20:00 UTC, CALIPSO detected ice (blue star symbol in Fig. 14 (a)) at a latitude of -77.42° and longitude of 49.96°, at a potential temperature of 366 K. Before this, CALIPSO observed liquid-NAT mixture along this trajectory at time, t = -21.7 h during 24-06-2020. During the observation of the liquid-NAT mixture, the temperature was around 195 K, which is ~3 K below $T_{NAT}$, and MLS measured gas-phase $HNO_3$ and $H_2O$ mixing ratios of 5.2 ppb and 5 ppm, respectively. CLaMS box model run indicated that the NAT has SAD of ~9 $\mu m^2$ $cm^{-3}$ (Fig. 14(e)). Approximately 14 hours later (i.e., at time t = -13 h), the temperature decreased below $T_{ice}$, and depletion of $H_2O$ started (Fig. 14 (d)). By the same time, ice SAD had started increasing

gradually (Fig. 14 (f)) and continued to increase as temperature decreased ~2.5 K below $T_{ice}$. This suggests the nucleation of ice on the NAT particles. A general good agreement is found between the total uptakes of $HNO_3$ and $H_2O$.

Case 6: NC precedes ice PSC

In this case, NC is observed before the observation of ice. On 19-06-2020, at 18:00 UTC, CALIPSO detected ice (blue star symbol in Fig. 15 (a)) at a latitude of -80.96° and longitude of 6.00°, at a potential temperature of 451 K. Before this, CALIPSO observed NC along this trajectory at the time, t = -37.6 h during 18-06-2020. During the observation of NC, the temperature was around 192.5 K, which is 1 K above $T_{NAT}$ (Fig. 15 (b)), and MLS measured gas-phase $HNO_3$ and $H_2O$ mixing ratios of 2 ppb and 3.7 ppm, respectively (Fig. 15 (c-d)). As the temperature is above $T_{NAT}$, there is no possibility of the formation of PSCs at this time. Approximately 14.6 hours later (i.e., at time t = - 13 h), a strong depletion in CLaMS $HNO_3$ is observed with CLaMS $H_2O$ mixing ratio unchanged as the temperature decreased below $T_{NAT}$. By the same time, NAT SAD has increased to ~2.7 $\mu m^2\ cm^{-3}$ (Fig. 15 (e)). At the time, t = -18 h, ice SAD started increasing gradually as the temperature reached $T_{ice}$ (Fig. 15 (f)) and reached a peak value of ~20 $\mu m^2\ cm^{-3}$. This suggests the nucleation of ice on the NAT particles.

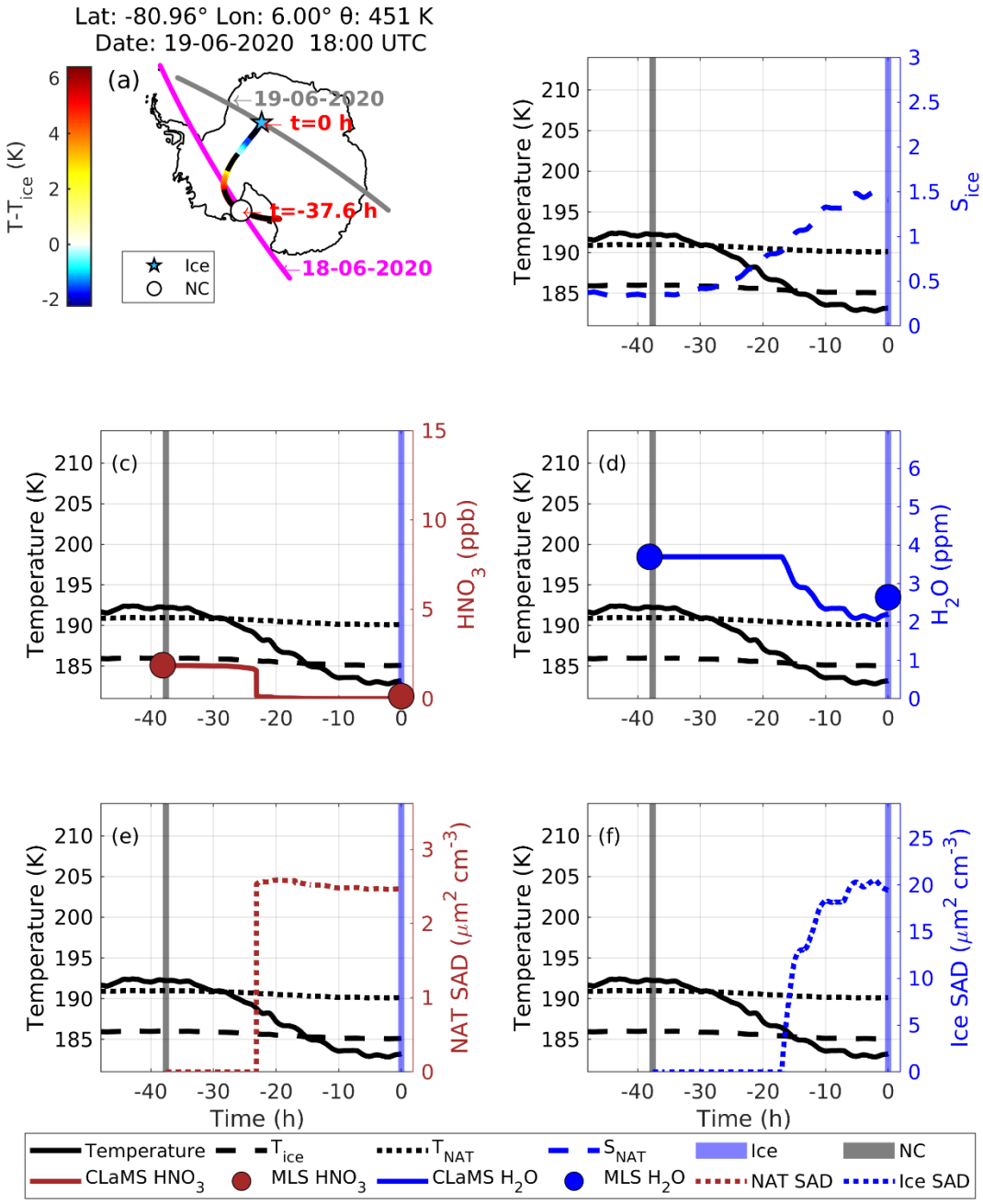


Figure 15. Same as Fig. 8 but for case no. 6 where ice nucleation on NAT is shown.

### 4.5.7 NAT-free ice formation

In this section, we discuss case no. 7 where the NAT-free ice nucleation process leads to ice formation.

Case 7: NC precedes ice PSC

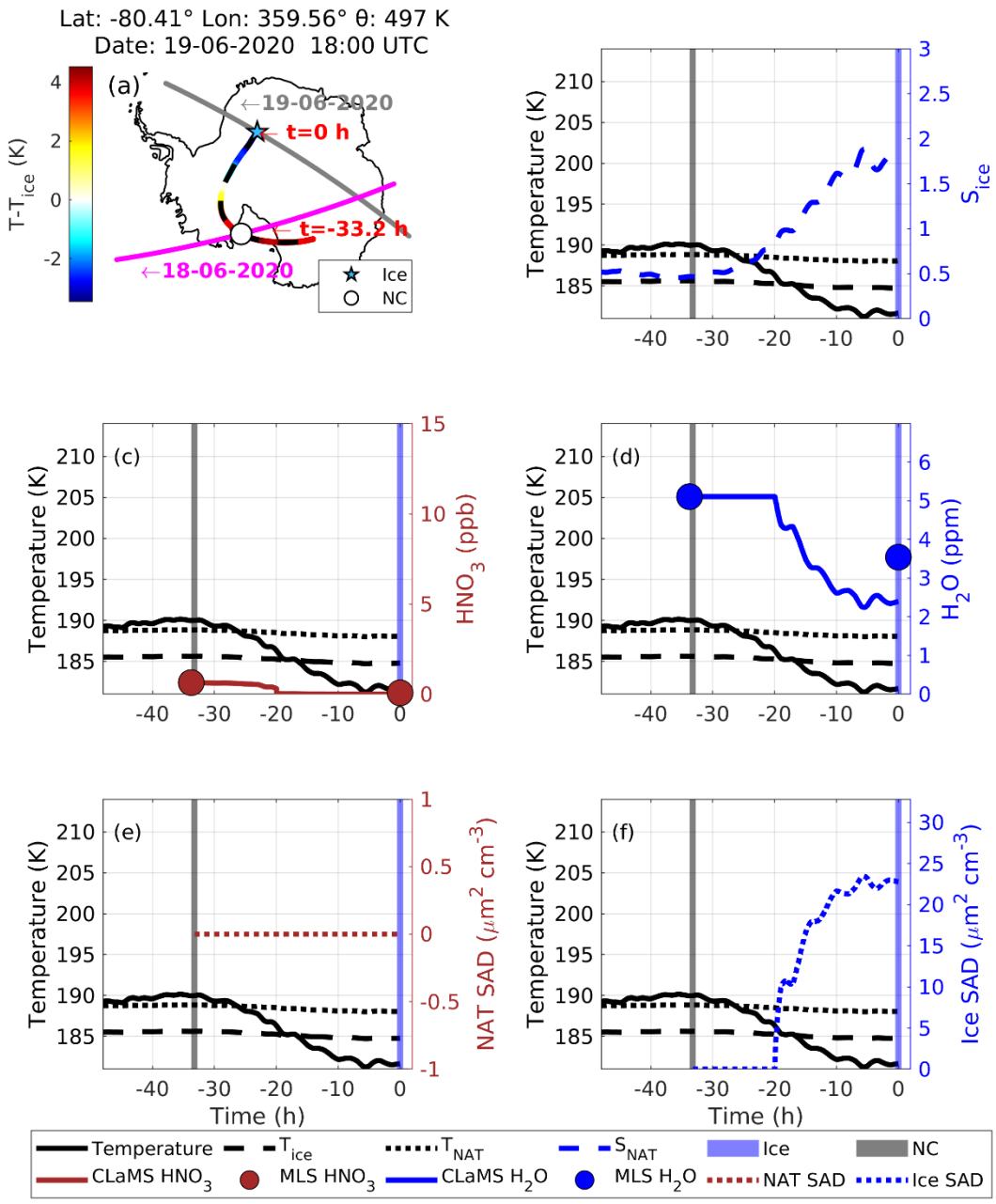


Figure 16. Same as Fig. 8 but for case no. 7 where ice nucleated without NAT.

There are notable similarities between case no. 6 and case no. 7. In both cases, the latitude, longitude, and temperature histories of the observed ice PSC and the preceding NC along the backward trajectory are almost identical. However, the ice PSC in case no. 7 is located at a potential temperature of 497 K (Fig. 16 (a)), whereas for case no. 6, it is at a relatively lower potential temperature of 451 K (Fig. 15 (a)). Despite having similar temperature histories, ice formed by nucleating on NAT in case no. 6, while in case no. 7, ice formed without NAT. A key difference between the two cases is the availability of gas-phase $HNO_3$. For case no. 7, the MLS $HNO_3$ mixing ratio at the CALIPSO NC observation is 0.6 ppb (denitrified scenario), which is 1.4 ppb lower than that of case no. 6. Hence, compared to case no. 6, for case no. 7 relatively low MLS $HNO_3$ is observed when the temperature was above $T_{NAT}$. The CLaMS box model for case no. 7 shows no NAT formation along the trajectory,

with NAT SAD remaining at 0 $\mu m^2$ $cm^{-3}$ (Fig. 16 (e)), while for case no. 6, NAT SAD increases to 2.7 $\mu m^2$ $cm^{-3}$ (Fig. 15 (e)). This is because, in case no. 7, there is not enough gas-phase $HNO_3$ (with just 0.6 ppb) to form NAT as it might have already been removed through the growth of NAT to large size, leading to denitrification before the observation of NC itself. In both cases, ice forms as the temperature drops below $T_{ice}$, with ice SAD reaching ~23 $\mu m^2$ $cm^{-3}$ in case no. 7 which is 3 $\mu m^2$ $cm^{-3}$ higher than in case no. 6 (Fig. 16 (f)). Furthermore, during ice formation, the maximum $S_{ice}$ is ~1.5 in case no. 6, compared to a high supersaturation $S_{ice}$ of 1.8 in case no. 7 (Fig. 16 (b)). Since ice can form through a homogeneous nucleation process at $S_{ice} > 1.5$, the temperature needs to be 3 K below $T_{ice}$. But for this case, the temperature is just 2 K below $T_{ice}$, suggesting heterogeneous nucleation of ice but without NAT. One possibility could be that STS with the inclusion of foreign nuclei could have served as the formation of ice in this case. As, the bushfire aerosols entered the lower stratosphere at the high-latitude region as shown in Fig. 1 and Fig. 2, it is highly likely that bushfire aerosols also included in the STS along with foreign nuclei. In short, under the denitrified scenario where there is not enough availability of gas-phase $HNO_3$, ice can form through the NAT-free nucleation process. Based on PSC measurement of lidar on board the HALO (High Altitude and Long Range Research Aircraft), Voigt et al., (2018) observed ice PSCs with a bimodal distribution of particle depolarization ratio on 22 January 2016 over the Arctic region., In which, Lagrangian backward trajectory analysis revealed that the ice with high depolarization ratio are preceded by NAT from CALIPSO measurement. Furthermore, ice with a low depolarization ratio are preceded by STS. Hence, to investigate the ice formation through NAT-free and NAT-assisted nucleation process cases, we analyzed the depolarization ratio of ice and discussed it in the next section.

#### 4.5.8 Bimodal distribution of depolarization ratio of ice PSC

The depolarization ratio of ice preceded by a liquid-NAT mixture and STS along the backward trajectories are analyzed, with the corresponding probability densities shown in Fig. 17. As discussed in case no. 2, after the CALIPSO observation of STS, it is possible that a liquid-NAT mixture formed as temperature decreases and these NAT acted as nuclei for ice formation. Therefore, the probability density for the STS case may reflect not only the formation of ice on STS but also ice nucleated on NAT. The probability density for ice preceded by a liquid-NAT mixture (solid red line in Fig. 17(a)) peak at 0.35. In contrast, the probability density for ice preceded by STS (solid black line in Fig. 17(a)) shows a bimodal distribution, with a high depolarization mode peaking at 0.26 and a low depolarization mode peaking at 0.07. This observation of the bimodal distribution of depolarization ratio is similar to the findings reported by Voigt et al., (2018). This bimodal distribution suggests that under certain conditions, ice nucleates on NAT/STS, contributing to the mixed depolarization signal. Through case no. 7, it is shown that under denitrified conditions, the ice can nucleate on STS with foreign nuclei inclusion instead of NAT.

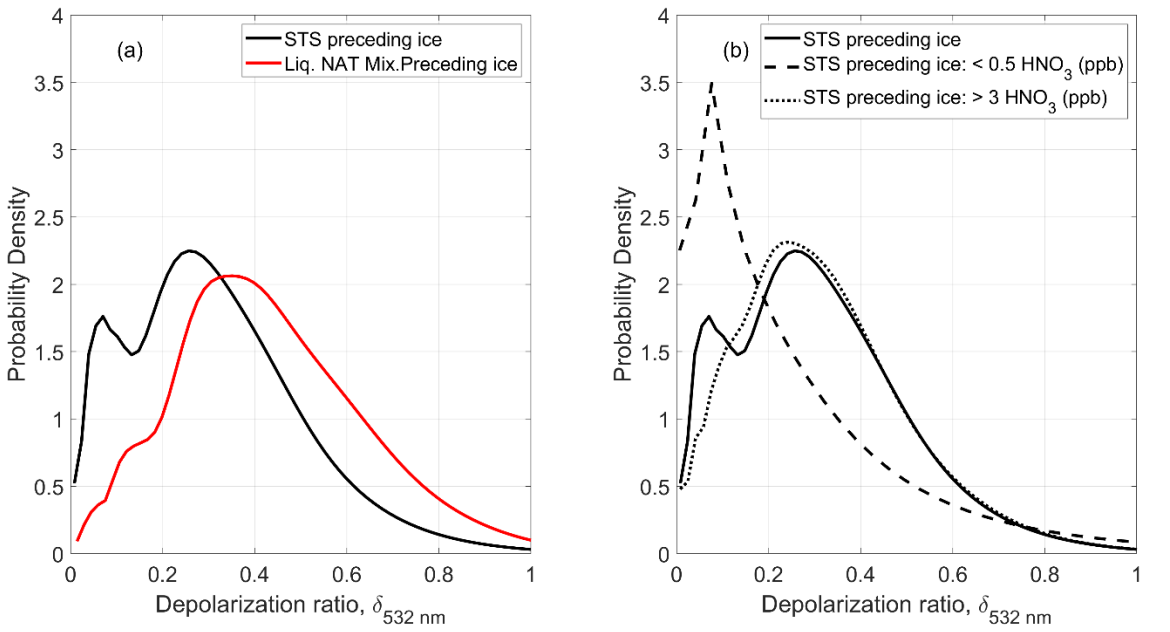


Figure 17. (a) The probability density of the depolarization ratio of ice preceded by STS (solid black line) and liquid-NAT mixture (solid red line) are shown. (b) decomposition of ice preceded by STS cases based on MLS $HNO_3$ mixing ratios: < 0.5 ppb (dashed line) and > 3 ppb (dotted line).

So, we chose ice PSCs which are preceded by STS under the denitrified condition of MLS $HNO_3$ < 0.5 ppb (i.e. during the observation of STS along the backward trajectory of ice, the MLS $HNO_3$ should be < 0.5 ppb), and under normal condition of MLS $HNO_3$ > 3.0 ppb. Figure 17 (b) shows the depolarization ratio of ice preceded by STS, distinguishing between cases under a denitrified scenario (MLS $HNO_3$ < 0.5 ppb, black dashed line), and under normal conditions (MLS $HNO_3$ > 3 ppb, black dotted line). These threshold values of 0.5 ppb and 3 ppb are chosen because they effectively separate the bimodal distribution into two clearly distinguishable modes. The lower threshold (0.5 ppb) captures the conditions where denitrification is significant, and NAT is less likely to form, leading to ice nucleation directly on STS with foreign nuclei inclusion. On the other hand, the higher threshold (3 ppb) represents conditions where sufficient $HNO_3$ is available for NAT formation, supporting ice nucleation via NAT-assisted processes. These thresholds help differentiate the distinct nucleation pathways reflected in the depolarization ratio distributions. The low $HNO_3$ case shows a more pronounced peak at lower depolarization values (~0.076), while the high $HNO_3$ case follows a distribution more similar to the overall STS case with a higher depolarization peak near 0.26. This suggests a potential influence of the availability of gas-phase $HNO_3$ on the ice nucleation processes. Under normal gas-phase $HNO_3$ available conditions, ice tends to form through NAT-assisted nucleation process, and under the denitrified condition where there is not enough $HNO_3$ to form NAT, ice can form through NAT-free nucleation process i.e., nucleating on STS with foreign nuclei inclusion.

### 4.5.9 Validation of $HNO_3$ and $H_2O$ uptakes during ice formation

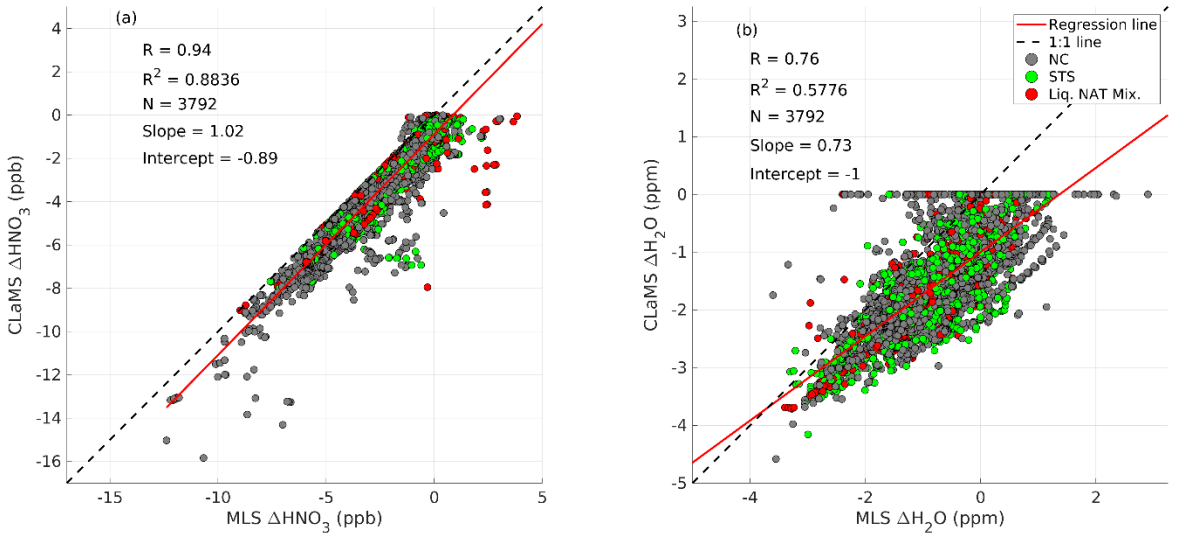


*Figure. 18. Same as Fig. 12. But for the case of ice formation.*

A strong correlation is found between the MLS observed change in $HNO_3$ ($\Delta HNO_3$) and the CLaMS modeled change in $HNO_3$, with a correlation coefficient (R) of 0.94 and a coefficient of determination ($R^2$) of 0.8836 (Fig. 18(a)). Similar to $HNO_3$ uptakes during the formation of liquid-NAT mixture from NC, significant $HNO_3$ uptake of up to 12 ppb, as observed by MLS, occurs when NC preceded the observation of the ice along the trajectory (indicated by the grey circle in Fig. 18(a)). In contrast, a relatively low $HNO_3$ uptake is noted when STS (liquid-NAT mixture) preceded the ice formation which is marked with the green circle (red circle) in Fig. 18(a). In the case of $H_2O$ uptake, a good correlation is found between MLS $\Delta H_2O$ and CLaMS $\Delta H_2O$, with a correlation coefficient (R) of 0.76 and a coefficient of determination ($R^2$) of 0.5776 (Fig. 12(b)).

### 4.5.10 Relative percentage contribution of ice formation pathways

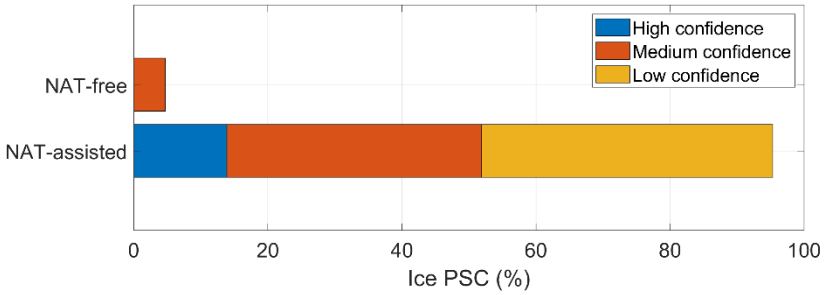


*Figure 19. The percentage of ice PSCs formed via NAT-assisted and NAT-free nucleation processes, categorized by confidence levels based on backward trajectory observations and MLS $HNO_3$ availability. The bars represent high, medium, and low confidence cases for each process, with confidence levels determined by the presence of NAT and gas-phase $HNO_3$ concentrations along the trajectories.*

Based on the Lagrangian backward trajectory analysis and availability of gas-phase $HNO_3$ as observed through MLS, we estimated the relative percentage contributions of NAT-assisted and NAT-free ice formation processes,

with the color-coded bars indicating different confidence levels based on observational evidence and shown in Fig 19. High confidence (blue) in NAT-assisted formation indicates that direct CALIPSO observational evidence of liquid-NAT mixture was found along the backward trajectory of the ice PSC. This provides strong evidence that the ice formed through NAT-assisted nucleation. Ice PSCs which formed via the NAT-assisted nucleation process are classified with medium confidence (orange) when there is no direct observation of NAT, but significant availability of gas-phase MLS $HNO_3$ >3 ppb during the observation of NC/STS along the backward trajectory. In this case, even without the detection of NAT, the availability of $HNO_3$ strongly suggests that NAT could have formed, justifying a medium confidence classification for NAT-assisted nucleation. Low confidence (yellow) in NAT-assisted formation corresponds to cases where the MLS $HNO_3$ mixing ratio during NC/STS observations was between 0.5 and 3 ppb. While NAT formation cannot be ruled out, the lower $HNO_3$ mixing ratio suggest only a low likelihood of NAT's involvement. Hence classifying these types of cases to NAT-assisted nucleation with low confidence.

Ice PSCs which formed during extreme denitrified conditions are classified as NAT-free ice formation with medium confidence. Here, the backward trajectories reveal very low MLS $HNO_3$ (<0.5 ppb), creating conditions where NAT formation is unlikely, and ice must have nucleated without the presence of NAT. In this scenario, ice PSCs are likely formed on STS particles with foreign nuclei inclusion. This breakdown helps to clarify the processes of ice formation under varying atmospheric conditions and enhances our understanding of the role NAT plays in polar stratospheric cloud nucleation. The clear separation into different confidence levels also emphasizes the influence of gas-phase $HNO_3$ availability on determining the nucleation pathway.

In summary, we report the strong enhancement in aerosol loading in the lower stratosphere caused by the black summer event during early 2020. In addition, we observed increased gas-phase MLS $HNO_3$ and $H_2O$ mixing ratio at an altitude of ~25 km and ~17 km respectively. The increased $HNO_3$ is due to enhanced heterogeneous reaction known as $N_2O_5$ hydrolysis while increased $H_2O$ is directly injected by smoke plumes from the bushfire. Subsequently, during Austral Winter 2020, anomalously high PSC areal coverage was observed, suggesting that the modified stratospheric composition of trace gases strongly influenced the PSC formation. Despite of relatively high availability of gas–phase $HNO_3$ during this period compared to previous normal years, the liquid–NAT mixture PSC remained within one standard deviation with respect to the background mean (2009–2019) while the ice PSC areal coverage exceeded three standard deviations. To explain this behavior, we calculated the 48 h backward trajectories of ice and liquid-NAT mixture PSCs using CLaMS trajectory module with hourly ERA5 operational analysis meteorological data. The temperature history, uptakes of MLS $HNO_3$, $H_2O$ mixing ratio during the formation of these ice/liquid–NAT mixture PSCs and types of PSC observed before the observation of these PSCs along the trajectories are studied to understand their formation pathways. Through this analysis, we report that 79 % of liquid-NAT mixture formed via ice-free nucleation pathway accounts with high confidence, as ice PSC is not observed along the trajectory as well as temperature of the air parcel never decreased 1.5 K below $T_{ice}$ (i.e., minimum temperature required for ice formation) from the time of observation of 'No Cloud (NC)'/STS till liquid-NAT mixture observation along the backward trajectory. This confirms no formation of ice before the observation of the liquid-NAT mixture. Whereas we report 12 % of liquid-NAT mixture formed via ice-assisted nucleation pathway with high confidence as ice PSC is observed through CALIPSO before the formation of liquid-NAT mixture along the trajectory and 9 % with low confidence as there is no direct CALIPSO

observation of ice PSC before the liquid-NAT mixture but the corresponding temperature decreased 1.5 K below $T_{ice}$, indicating possible involvement of ice during this liquid-NAT mixture formation.

In the case of ice formation, we observed that depolarization ratio at 532 nm of ice PSCs preceded by STS along the trajectories exhibited bimodal distribution. The low depolarization ratio mode peaked at 0.07, and high depolarization ratio mode peaked at 0.26. In contrast, the ice PSC preceded by liquid-NAT mixture along the trajectory exhibited single mode of depolarization ratio with peak occurred at 0.35 which is closer to the high depolarization ratio mode of ice PSC preceded by STS. This hints that ice with high depolarization ratio could be result of nucleation of ice on NAT particle and low depolarization ratio to nucleation of ice on STS which is supported by previous study from Voigt et al., (2018). To check this, we analyzed the availability of gas-phase $HNO_3$ at the time of observation of STS, which was observed before ice formation along the backward trajectories, as $HNO_3$ availability is crucial for NAT formation. The results indicate that ice PSCs with low depolarization ratios formed under denitrified conditions, where MLS $HNO_3$ mixing ratio were below 0.5 ppb during the STS observation along the backward trajectories. In these conditions, NAT particles could not form due to low $HNO_3$ availability which is also confirmed by CLaMS box model run and resulted in ice nucleating directly on STS. In contrast, ice PSCs with high depolarization ratios formed under normal conditions, where MLS $HNO_3$ mixing ratio exceeded 3 ppb during the STS observation. This enough availability of gas-phase $HNO_3$ led to formation of NAT particles (again, this is also confirmed by CLaMS box model run) and led to ice nucleating on NAT. Hence, based on the availability of gas-phase MLS $HNO_3$ and temperature history, we conclude the ice formation pathways and relatively percentage contribution of formation pathways.

Hence, we report that 13.86 % of ice is formed through NAT-assisted ice formation with high confidence as direct CALIPSO observations of liquid-NAT mixtures are present along the trajectory. And 38.02 % with medium confidence, as there is significant gas-phase MLS $HNO_3$ (>3 ppb) suggesting possible NAT formation before the ice formation. And 43.42 % with low confidence when $HNO_3$ levels are between 0.5 and 3 ppb, indicating a lower likelihood of NAT formation. Furthermore, we report that only 4.69 % of ice formed through NAT-free ice formation with medium confidence, as they are formed under extremely denitrified conditions ($HNO_3$ < 0.5 ppb), suggesting less likelihood of NAT formation and thus ice formed through nucleating on STS. This suggests, availability of the gas-phase $HNO_3$ is crucial factor in deciding whether ice forms through NAT-assisted or NAT-free nucleation process. To the best of our knowledge, this is the first study which provides relative contributions of various liquid-NAT mixtures and ice formation pathways. These results provide deeper insights into the microphysical processes through which the aerosols from extreme bushfire events (like black summer) can influence stratospheric chemistry and PSC formation.

~~3.5.1 LNAT formation pathways~~

~~The change in air temperature (ΔT), $HNO_3$ ($\Delta HNO_3$), and temperature ($T - T_{ice}$) at which transition in PSC composition is observed are shown respectively in Fig. 10 and Fig. 11. The negative and positive values of 'ΔT' ('$\Delta HNO_3$') indicate the cooling (uptake) and warming (release) of the air parcels (gas-phase $HNO_3$). As 'ΔT' and '$\Delta HNO_3$' exhibit skewed distributions (not shown here), their median values are chosen to represent the average~~ (Huff, 2023)~~.~~

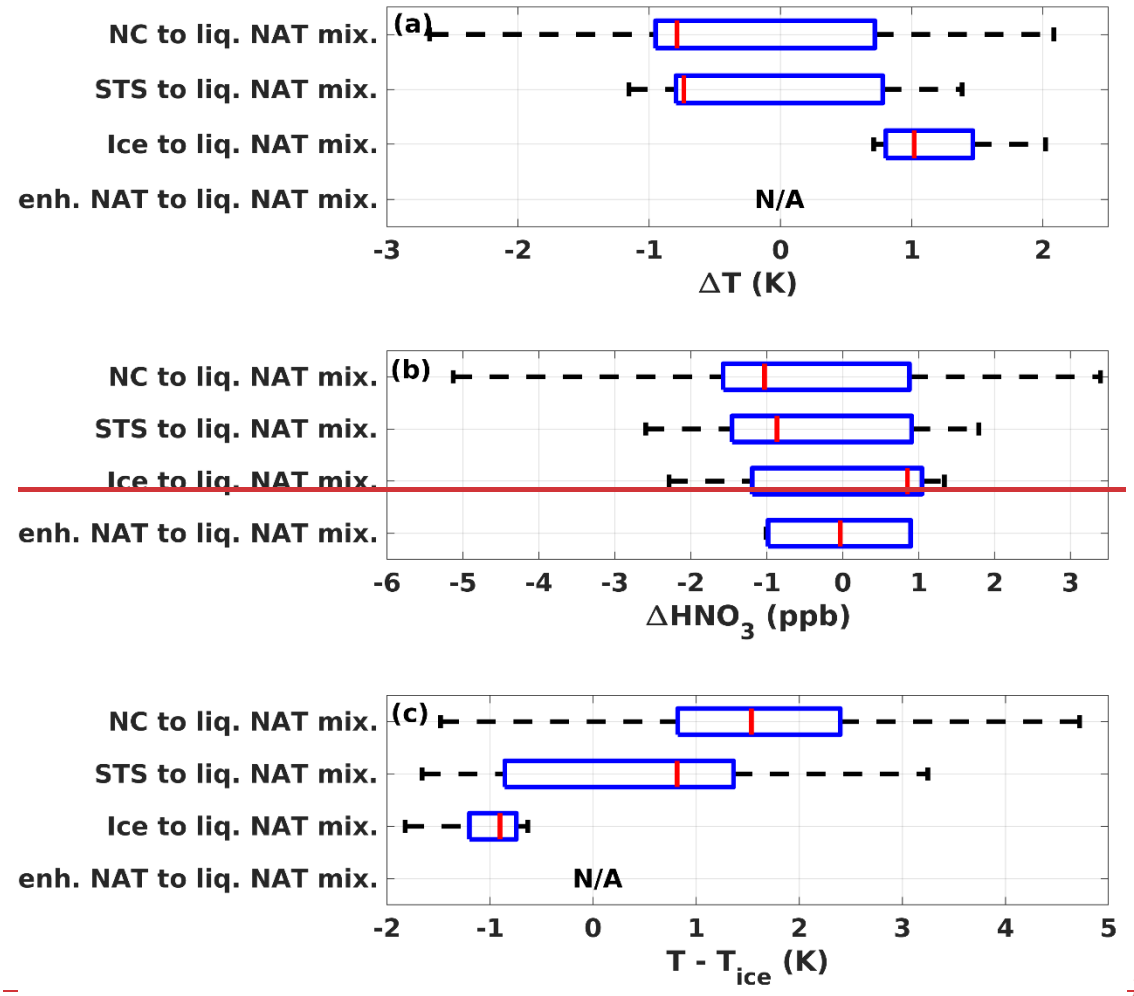


~~*Figure 10: Observed change in (a) temperature (ΔT) and (b) $HNO_3$ ($\Delta HNO_3$) of the air parcels in which various formation pathways leading to LNAT formation are shown. The temperature at which LNAT forms is shown on the $T - T_{ice}$ temperature coordinate in panel (c). 'N/A' represents no availability of data. In the boxplot, the redline marks the median of the respective quantities, and the left and right whiskers represent the minimum and maximum of the observed changes, respectively.*~~

~~The results in Fig. 9 b show that 82 % of LNAT is formed through the 'NC to LNAT' pathway, during which the corresponding air parcels are cooled (average ΔT = -0.75 K) as seen in Fig. 10a and led to the uptake of $HNO_3$ (average $\Delta HNO_3$ = -0.8 ppbv) as seen in Fig. 10b. Though, according to CALIPSO PSC classification, NC refers to 'No Cloud' detected, it may yet contain either (i) stratospheric liquid sulfate aerosol immersed with foreign nuclei (such as meteoritic dust or smoke aerosols) or (ii) large NAT at very low number density, such that their optical signal is below the detection threshold of CALIPSO~~ (Lambert et al., 2012, 2016)~~. The former scenario leads to PSC formation through the uptake of $HNO_3$ (upon cooling of the air), and the latter leads to denitrification, which increases gas-phase $HNO_3$ (upon warming). Given an observed cooling and uptake of $HNO_3$, we consider that 'NC' primarily corresponds to the presence of stratospheric aerosols rather than large NAT. Furthermore, as stated earlier, the LNAT is a mixture of liquid STS and solid NAT~~ (Pitts et al., 2011)~~. The liquid STS can form through a homogeneous nucleation process from Stratospheric Sulfuric Acid (SSA; $H_2SO_4.H_2O$) which is ubiquitous in the stratosphere~~ (Junge et al., 1961)~~. As the temperature decreases, the SSA transforms into STS homogeneously, upon the uptake of $H_2O$ and $HNO_3$~~ (Carslaw et al., 1994)~~. Observational evidence based on ground-based lidar data supports the formation of STS through homogeneous nucleation~~ (Biele et al., 2001)~~. Hence, owing to the observed decrease in temperature and gas-phase $HNO_3$, we primarily attribute the formation of liquid STS in the LNAT mixture to the homogeneous nucleation process.~~

~~Unlike STS, the homogeneous nucleation of NAT is kinetically suppressed~~ (Koop et al., 1995)~~. Thus, the heterogeneous nucleation processes such as (i) ice-induced NAT nucleation and (ii) ice-free NAT nucleation are the possible ways of solid NAT formation. The former requires the presence of ice PSC which occurs only when the temperature T-$T_{ice}$ < 0~~ (Carslaw et al., 1999)~~. The latter requires the presence of solid foreign nuclei such as meteoritic dust, volcanic ash, soot, or $H_2SO_4$ hydrates which occurs even when the temperature is above T-$T_{ice}$~~ (Iraci et al., 1995; Peter and Grooß, 2012)~~. We noticed that the majority of the LNAT is formed via the 'NC-to-LNAT' pathway at temperatures T-$T_{ice}$ > 0, averaging around T-$T_{ice}$ = 1.6 K (Fig. 10c). Thus, the ice-free nucleation process is the primary cause of the observed LNAT formation rather than the ice-induced nucleation process, which is further substantiated by the observed uptake of $HNO_3$ and cooling of the air parcels.~~

~~We have observed that 15 % of the LNAT is formed through the 'Ice-to-LNAT' pathway (Fig. 9b), where the corresponding air parcels are found to be warming (average ΔT = 0.8 K; Fig. 10a) and led to the release of $HNO_3$ (average $\Delta HNO_3$ = 0.9 ppbv; Fig. 10b). It occurred at a temperature of T-$T_{ice}$ = -0.9 K (Fig. 10c). These observations rule out the possibility of heterogeneous nucleation of LNAT on ice, which occurs only after homogeneous nucleation of ice and requires T-$T_{ice}$ < -3 Hence, the average ΔT and temperature at which LNAT is formed indicate that it is likely that the ice already nucleated on LNAT, and upon warming, the ice evaporated, leading to the exposure of the LNAT.~~

~~In the case of the 'STS to LNAT' pathway, which is responsible for 2.8 % of LNAT formation (Fig. 9b), the corresponding air parcels are found to be cooling (average $\Delta T = -0.7$ K) and resulted in condensation of $HNO_3$ (average $\Delta HNO_3 = -0.85$ ppbv) (Fig. 10a, b). Laboratory experiments have revealed that the homogeneous nucleation rate of NAT on STS is extremely low for stratospheric conditions~~ (Hanson and Ravishankara, 1991; 1992)~~. However, the STS, with the inclusion of foreign nuclei, can potentially serve as nuclei for NAT formation~~ (Koop et al., 1997)~~. Ground-based lidar observations by~~ Biele et al. (2001) ~~provided evidence of the existence of such STS with foreign nuclei inclusion. As such, solid NAT would have nucleated on STS with foreign nuclei inclusion and thus transformed STS into LNAT mixture. A very meager fraction of the ENAT (~0.7 %) was transformed to LNAT and since there is no valid corresponding temperature data, the formation process is inconclusive.~~

~~3.5.2 Ice formation pathways~~

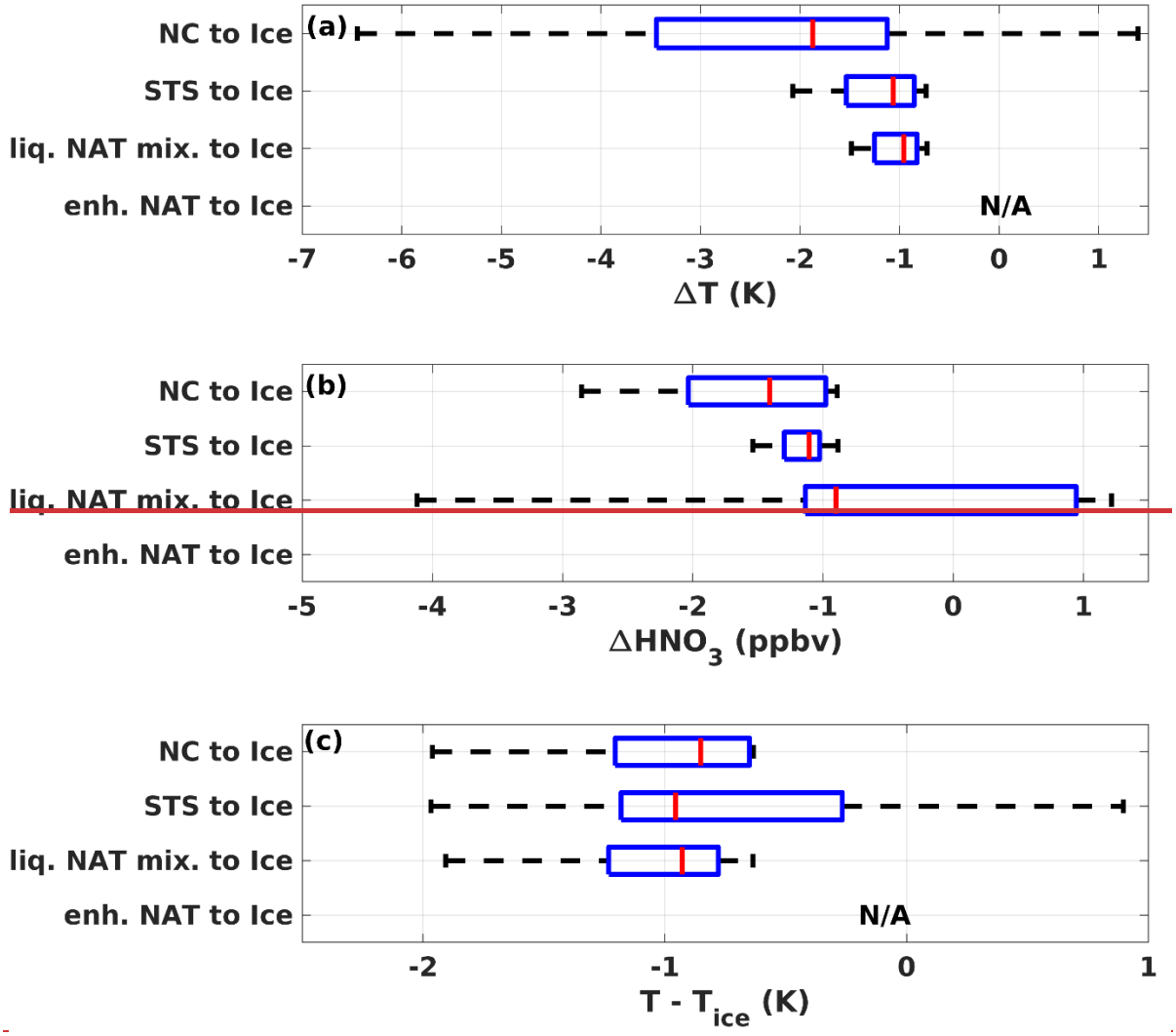

~~*Figure 11: Same as Fig. 10 but for the case of ice PSC.*~~

~~Figure 9d reveals that the most dominant formation pathway for ice formation is 'LNAT-to-Ice' (77 %), during which average ΔT is found to be ~1 K, indicating cooling of the corresponding air parcels. The average $\Delta HNO_3$ is found to be ~0.9 ppbv, indicating an uptake of $HNO_3$ (Fig. 11 a, b). It occurred at the temperature of T-$T_{ice}$ = ~0.95 K (Fig. 11 c). The NAT is known to act as potential nuclei for ice formation~ (Khosrawi et al., 2011; Engel et al., 2013; Voigt et al., 2018)~~. Hence, based on the observed change in temperature and the temperature at which the ice formed, the ice nucleating on the existing LNAT is the most feasible pathway.~~

~~Following the LNAT-to-Ice pathway, 17 % of the ice is formed through the 'NC-to-Ice' pathway (Fig. 9d). During the ice formation through this pathway, a relatively rapid decrease in temperature, with an average ΔT of ~1.9 K and a maximum cooling of ~6.5 K, is observed (Fig. 11a). Furthermore, an uptake of $HNO_3$ with an average $\Delta HNO_3$ of ~1.4 ppbv is also observed (Fig. 11b). While homogeneous nucleation of ice is another possibility, it occurs only under supercooled conditions at temperatures between T-$T_{ice}$ = ~3 K and T-$T_{ice}$ = ~4 K~ (Koop et al., 1998)~~. But the observed temperature at which these ices are formed never fell below T-$T_{ice}$ = ~2 K, ruling out the possibility of homogeneous ice nucleation (Fig. 11c). It indicates that the 'NC-to-Ice' is possibly a tandem of two pathways described above: 'NC-to-LNAT' and 'LNAT-to-Ice'~ (Peter, 1997)~~. Due to the rapid temperature decrease, both these processes probably occurred in a relatively shorter time frame.~~

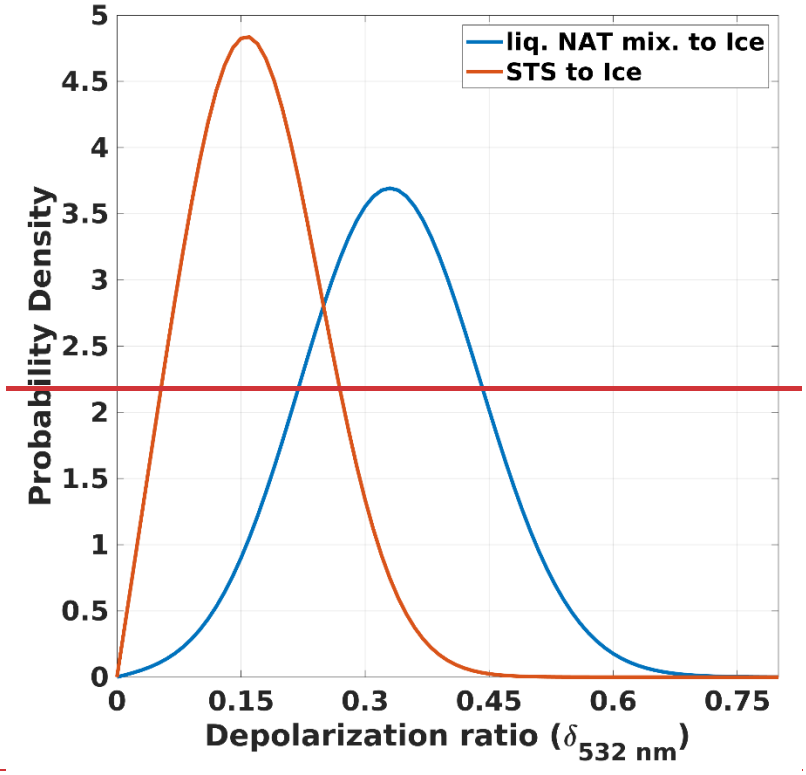

~~*Figure 12: Probability density of the CALIPSO PSC depolarization ratio ($\delta_{532\ nm}$) for ice formed through the 'LNAT-to-Ice' pathway (blue line), and 'STS-to-Ice' pathway (orange line).*~~

~~We observed just 5.1 % of the ice is formed through the 'STS-to-Ice" pathway (Fig. 9d). This process occurred at the temperature T-$T_{ice}$ = -0.95 K with an average ΔT and $\Delta HNO_3$ of -0.7 K, and -0.9 ppbv respectively (Fig. 11a, b). Similar to the 'STS-to-LNAT' pathway, the STS with solid nuclei inclusion could serve as nuclei for ice formation~~ (Koop et al., 1998; 2000; Engel et al., 2013)~~. The temperature at which this pathway has taken place indicates that the heterogeneous nucleation of ice on STS, with solid nuclei inclusion, could be a possible formation mechanism. Furthermore, we observed that the mean particulate depolarization ratio ($\delta_{532}$) of ice nucleated on STS ('STS-to-Ice' pathway) is 0.15, which is less than half of the depolarization ratio of ice ($\delta_{532}$~0.36) nucleated on LNAT ('LNAT-to-Ice' pathway; Fig. 12). This observation is consistent with the results from a previous aircraft campaign conducted over Arctic PSC, where the authors showed that $\delta_{532}$ of ice PSC exhibited bimodal distribution and ice formed through the 'STS-to-Ice' pathway has relatively low $\delta_{532}$ compared to the ice formed through 'LNAT-to-Ice' pathway~~ (Voigt et al., 2018)~~. It is possible because STS is always in the liquid state and has a spherical shape, leading to low $\delta_{532}$. Hence the ice nucleation on the STS is also likely to lead to 'near-spherical' morphology. On the other hand, LNAT always exists in the solid state, and due to its non-spherical morphology, $\delta_{532}$ tends to be relatively larger than that of STS. The rest of the ice (2 %) is formed through the 'ENAT-to-Ice' pathway. Since there is no valid data for the corresponding thermodynamics parameters, further discussion on this is omitted.~~

~~From the above discussions, it is clear that the majority of the LNAT (82 %) and ice (77 %) are formed through 'NC-to-LNAT' and 'LNAT-to-Ice' pathways respectively. It indicates that LNAT nucleated on the stratospheric aerosols, which subsequently acted as nuclei for ice formation. Moreover, the 'LNAT-to-Ice' conversion should have occurred rapidly to explain the high anomalous ice areal coverage. In fact, both 'NC-to-LNAT' and 'LNAT-to-Ice' pathways are parts of the three-stage PSC formation model~~ (Peter, 1997)~~. During the first stage, the heterogeneously nucleated solid $H_2SO_4$ hydrates on other foreign nuclei such as meteoritic dust, soot, etc. present in the atmosphere~~ (Luo et al., 1994)~~. Along with these nuclei, aerosols from the black summer event also participated in this stage during Austral winter 2020. In the second stage, these nuclei lead to heterogeneous nucleation of solid NAT, and in the third stage, upon cooling further, the ice nucleates on the pre-existing NAT~~ (Peter, 1997; Lowe and MacKenzie, 2008)~~. These results corroborate the hypothesis which we made earlier that majority of the Antarctic ice PSC forms by nucleating on the pre-existing NAT PSC.~~

~~In summary, we report the strong enhancement in aerosol loading in the lower stratosphere caused by the black summer event. In early 2020, it significantly affected the stratospheric chemistry by promoting increased production of $HNO_3$ at an altitude of ~25 km and directly injecting $H_2O$ at an altitude of ~17 km. Subsequently, during Austral Winter 2020, anomalously high PSC areal coverage was observed, which conveys that the modified stratospheric chemistry strongly influenced the PSC formation. Furthermore, we observed that the ice areal coverage exceeded three standard deviations with respect to the background mean while the LNAT remained within one standard deviation. To explain this behavior, we developed a novel methodology which retrieves the~~

~~relative contribution of various PSC formation pathways from satellite measurements. The results revealed that most of the LNAT is formed via a heterogeneous nucleation process assisted by the aerosols from the black summer event. Subsequently, these LNAT rapidly acted as nuclei for ice formation, resulting in anomalous high areal coverage of ice PSC. The consistency of the observed thermodynamics of the PSC formation process with our existing knowledge indicates that our methodology could efficiently retrieve the PSC formation pathways using satellite measurements. To the best of our knowledge, this is the first study which provides relative contributions of various LNAT and ice formation pathways. These results provide deeper insights into the microphysical processes through which the aerosols from extreme bushfire events (like black summer) can influence the stratospheric chemistry and PSC formation.~~

## ~~4~~5 Conclusions

Australia's extreme bushfire event of 2019/20, also referred to as black summer, injected 0.4 to 2 Tg of aerosols into the stratosphere, initiating a series of events. We carried out an extensive investigation on the impacts of bushfire emissions on the Polar Stratospheric Clouds (PSCs), using multi-satellite and reanalyses data. In addition, to explain the anomaly observed in ice and liquid-NAT mixture PSC areal coverage, we studied the formation pathways of these PSCs by analysis temperature history, availability of gas-phase $HNO_3$, along with CLaMS microphysical box model simulation and retrieved the relative percentage contribution of formation pathways of ice and liquid-NAT mixture pathways. The key findings from this study are:

1. During the austral autumn of 2020, we found a significant increase in gas phase nitric acid ($HNO_3$) and water vapor ($H_2O$) (principal constituents of PSCs) from MLS measurement in high latitude region of the southern hemisphere at the altitudes of ~25 and ~17 km respectively. The former is due to the enhanced dinitrogen pentoxide hydrolysis process, caused by the increased bushfire aerosols. The latter is attributed to the direct injection of ~~the water~~water vapor by the black summer event.

2. The increase in $HNO_3$ was expected to enhance $HNO_3$-containing PSCs like STS and NAT. While the areal coverage of STS peaked significantly, no notable enhancement in liquid-NAT mixtures ~~LNAT~~ was observed. However, there was an anomalous increase in the areal coverage of ice PSC.

3. We report 79 % of liquid-NAT mixtures formed through ice-free nucleation with high confidence, as no ice PSCs observed along the backward trajectories and temperature remained above the ice formation threshold ($T_{ice}$-1.5K). Whereas 12 % of liquid-NAT mixtures formed via ice-assisted nucleation with high confidence, as CALIPSO observations of ice PSCs before liquid-NAT formation and 9% with low confidence, as the temperature dropped below the ice formation threshold but no direct ice PSC observation.

4. We observed bimodal distribution of depolarization ratio at 532 nm of ice PSCs which are preceded by STS along the backward trajectories. Further analysis on this revealed that, the low depolarization ratio mode (peaked at ~0.07) corresponds to ice nucleation on STS under denitrified conditions ($HNO_3$ < 0.5 ppb). High depolarization ratio (peaked ~0.26) corresponds ice nucleation on NAT under normal conditions ($HNO_3$ > 3 ppb).

5. We report 13.86 % of ice PSCs formed via NAT-assisted nucleation with high confidence, as presence of liquid-NAT mixtures are observed through CALIPSO along the backward trajectory of these ice PSCs and 38.02 % with medium confidence, as there is no direct CALIPSO observation of present of liquid-NAT mixture but significant $HNO_3$ availability > 3 ppb, hence high likelihood of NAT formation, and 43.42 % with low confidence, $HNO_3$ levels between 0.5 and 3 ppb, relatively low likelihood of the NAT. Thus, NAT-assisted ice formation pathway accounting for ~95 % of ice PSC. And just 4.69% of ice PSCs formed via NAT-free nucleation under extremely denitrified conditions ($HNO_3$ < 0.5 ppb), as not enough $HNO_3$ availability for NAT formation and thus these ice PSCs should have nucleated on STS with possible inclusion of foreign nuclei. These results suggest the ice formation pathway is also decided by the gas-phase $HNO_3$ availability.

~~Most of the LNAT (~82 %) were formed through heterogeneous nucleation on bushfire aerosols. Consequently, these LNAT served as nuclei for 77 % of ice PSC formation. This rapid conversion of LNAT to ice was responsible for the anomalous high areal coverage of ice PSC.~~

In the context of climate change scenarios, a warming troposphere and cooling stratosphere are ~~anticipated~~expected. The former is expected to increase the frequency of extreme wildfire events and the latter is projected to enhance the PSC areal coverage, together possibly delaying the ozone recovery process. The findings from this study will contribute to a deeper understanding of the influence of extreme wildfire events on PSC dynamics.

**Data availability**

Processed data are available upon request.

**Author contribution**

SP conceived the work and carried out the scientific data analysis. SP, NSA, KS, KKM, and SKS were involved in the scientific interpretation of the results, leading to the formulation of the manuscript. SP prepared the initial draft with input from NSA. All authors reviewed the manuscript.

**Competing interests**

The authors declare that they have no conflict of interest.

**Acknowledgements.**

We acknowledge the mission scientists of OMPS (for aerosol extinction coefficient, and temperature), MLS (for $HNO_3$, and $H_2O$ mixing ratio), ACE-FTS (for $HNO_3$, $H_2O$, HF, and $N_2O_5$ mixing ratio), ERA5 (for meteorological data), CALIPSO (for PSCs) and the associated personnel for the data used in this work. In addition, we acknowledge the CLaMS team for the model used in this work.

**Financial support**

One of the authors (SP) would like to thank the Centre for Research, Christ University for their support during this work. One of the authors (SKS) would like to thank SERB-DST for the J. C. Bose Fellowship. One of the authors (NSA) is supported by the DST in the form of an INSPIRE Faculty Fellowship (faculty registration number: IFA20-EAS-83). We thank the Divecha Centre for Climate Change for supporting this work.

**Review statement**

We thank the three anonymous reviewers and Dr.  Dr. Farahnaz Khosrawi for helping to improve the paper.

**References**

Allen, D. R., Fromm, M. D., Kablick III, G. P., and Nedoluha, G. E.: Smoke with induced rotation and lofting (SWIRL) in the stratosphere, J Atmos Sci, 77, 4297–4316, 2020.

Ansmann, A., Ohneiser, K., Chudnovsky, A., Knopf, D. A., Eloranta, E. W., Villanueva, D., Seifert, P., Radenz, M., Barja, B., Zamorano, F., Jimenez, C., Engelmann, R., Baars, H., Griesche, H., Hofer, J., Althausen, D., and Wandinger, U.: Ozone depletion in the Arctic and Antarctic stratosphere induced by wildfire smoke, Atmos Chem Phys, 22, 11701–11726, https://doi.org/10.5194/ACP-22-11701-2022, 2022.

Bernath, P. F., Steffen, J., Crouse, J., and Boone, C. D.: Atmospheric Chemistry Experiment SciSat Level 2 Processed Data, v4.0, 2020.

Biele, J., Tsias, A., Luo, B. P., Carslaw, K. S., Neuber, R., Beyerle, G., and Peter, T.: Nonequilibrium coexistence of solid and liquid particles in Arctic stratospheric clouds, Journal of Geophysical Research: Atmospheres, 106, 22991–23007, https://doi.org/10.1029/2001JD900188, 2001.

Bogdan, A. and Kulmala, M.: Aerosol silica as a possible candidate for the heterogeneous formation of nitric acid hydrates in the stratosphere, Geophys Res Lett, 26, 1433–1436, 1999.

Bogdan, A., Molina, M. J., Kulmala, M., MacKenzie, A. R., and Laaksonen, A.: Study of finely divided aqueous systems as an aid to understanding the formation mechanism of polar stratospheric clouds: Case of HNO3/H2O and H2SO4/H2O systems, Journal of Geophysical Research: Atmospheres, 108, 2003.

Brewer, A. W.: Evidence for a world circulation provided by the measurements of helium and water vapour distribution in the stratosphere, Quarterly Journal of the Royal Meteorological Society, 75, 351–363, https://doi.org/10.1002/QJ.49707532603, 1949.

Butchart, N.: The Brewer-Dobson circulation, Reviews of Geophysics, 52, 157–184, https://doi.org/10.1002/2013RG000448, 2014.

Carslaw, K. S., Luo, B. P., Clegg, S. L., Peter, T., Brimblecombe, P., and Crutzen, P. J.: Stratospheric aerosol growth and HNO3 gas phase depletion from coupled HNO3 and water uptake by liquid particles, Geophys Res Lett, 21, 2479–2482, https://doi.org/10.1029/94GL02799, 1994.

Carslaw, K. S., Peter, T., Bacmeister, J. T., and Eckermann, S. D.: Widespread solid particle formation by mountain waves in the Arctic stratosphere, Journal of Geophysical Research: Atmospheres, 104, 1827–1836, https://doi.org/10.1029/1998JD100033, 1999.

Chang, D. Y., Yoon, J., Lelieveld, J., Park, S. K., Yum, S. S., Kim, J., and Jeong, S.: Direct radiative forcing of biomass burning aerosols from the extensive Australian wildfires in 2019–2020, Environmental Research Letters, 16, 044041, https://doi.org/10.1088/1748-9326/ABECFE, 2021.

Curtius, J., Weigel, R., Vössing, H.-J., Wernli, H., Werner, A., Volk, C.-M., Konopka, P., Krebsbach, M., Schiller, C., and Roiger, A.: Observations of meteoric material and implications for aerosol nucleation in the winter Arctic lower stratosphere derived from in situ particle measurements, Atmos Chem Phys, 5, 3053–3069, 2005.

Cziczo, D. J., Thomson, D. S., and Murphy, D. M.: Ablation, Flux, and Atmospheric Implications of Meteors Inferred from Stratospheric Aerosol, Science (1979), 291, 1772–1775, https://doi.org/10.1126/SCIENCE.1057737, 2001.

Deb, P., Moradkhani, H., Abbaszadeh, P., Kiem, A. S., Engström, J., Keellings, D., and Sharma, A.: Causes of the Widespread 2019–2020 Australian Bushfire Season, Earths Future, 8, e2020EF001671, https://doi.org/https://doi.org/10.1029/2020EF001671, 2020.

Engel, I., Luo, B. P., Pitts, M. C., Poole, L. R., Hoyle, C. R., Grooß, J. U., Dörnbrack, A., and Peter, T.: Heterogeneous formation of polar stratospheric clouds-Part 2: Nucleation of ice on synoptic scales, Atmos Chem Phys, 13, 10769–10785, https://doi.org/10.5194/ACP-13-10769-2013, 2013.

Fueglistaler, S., Dessler, A. E., Dunkerton, T. J., Folkins, I., Fu, Q., and Mote, P. W.: Tropical tropopause layer, Reviews of Geophysics, 47, https://doi.org/10.1029/2008RG000267, 2009.

Gao, R. S., Gierczak, T., Thornberry, T. D., Rollins, A. W., Burkholder, J. B., Telg, H., Voigt, C., Peter, T., and Fahey, D. W.: Persistent Water-Nitric Acid Condensate with Saturation Water Vapor Pressure Greater than That of Hexagonal Ice, Journal of Physical Chemistry A, 120, 1431–1440, https://doi.org/10.1021/ACS.JPCA.5B06357/ASSET/IMAGES/MEDIUM/JP-2015-063578_0010.GIF, 2016.

Hanson, D. and Mauersberger, K.: Laboratory studies of the nitric acid trihydrate: Implications for the south polar stratosphere, Geophys Res Lett, 15, 855–858, https://doi.org/10.1029/GL015I008P00855, 1988.

Hanson, D. R. and Ravishankara, A. R.: The reaction probabilities of ClONO2 and N2O5 on 40 to 75% sulfuric acid solutions, Journal of Geophysical Research: Atmospheres, 96, 17307–17314, https://doi.org/10.1029/91JD01750, 1991.

Hanson, D. R. and Ravishankara, A. R.: Investigation of the reactive and nonreactive processes involving nitryl hypochlorite and hydrogen chloride on water and nitric acid doped ice, J Phys Chem, 96, 2682–2691, 1992.

Heinold, B., Baars, H., Barja, B., Christensen, M., Kubin, A., Ohneiser, K., Schepanski, K., Schutgens, N., Senf, F., and Schrödner, R.: Important role of stratospheric injection height for the distribution and radiative forcing of smoke aerosol from the 2019/2020 Australian wildfires, Atmospheric Chemistry and Physics Discussions, 1–20, 2021.

Hersbach, H., Bell, B., Berrisford, P., Hirahara, S., Horányi, A., Muñoz-Sabater, J., Nicolas, J., Peubey, C., Radu, R., Schepers, D., Simmons, A., Soci, C., Abdalla, S., Abellan, X., Balsamo, G., Bechtold, P., Biavati, G., Bidlot, J., Bonavita, M., De Chiara, G., Dahlgren, P., Dee, D., Diamantakis, M., Dragani, R., Flemming, J., Forbes, R., Fuentes, M., Geer, A., Haimberger, L., Healy, S., Hogan, R. J., Hólm, E., Janisková, M., Keeley, S., Laloyaux, P., Lopez, P., Lupu, C., Radnoti, G., de Rosnay, P., Rozum, I.,

Vamborg, F., Villaume, S., and Thépaut, J. N.: The ERA5 global reanalysis, Quarterly Journal of the Royal Meteorological Society, 146, 1999–2049, https://doi.org/10.1002/QJ.3803, 2020.

Hirsch, E. and Koren, I.: Record-breaking aerosol levels explained by smoke injection into the stratosphere, Science (1979), 371, 1269–1274, 2021.

Höpfner, M., Luo, B. P., Massoli, P., Cairo, F., Spang, R., Snels, M., Di Donfrancesco, G., Stiller, G., Von Clarmann, T., and Fischer, H.: Spectroscopic evidence for NAT, STS, and ice in MIPAS infrared limb emission measurements of polar stratospheric clouds, Atmos Chem Phys, 6, 1201–1219, 2006.

Hoyle, C. R., Engel, I., Luo, B. P., Pitts, M. C., Poole, L. R., Grooß, J. U., and Peter, T.: Heterogeneous formation of polar stratospheric clouds-Part 1: Nucleation of nitric acid trihydrate (NAT), Atmos Chem Phys, 13, 9577–9595, https://doi.org/10.5194/ACP-13-9577-2013, 2013.

Iannarelli, R. and Rossi, M. J.: The mid-IR Absorption Cross Sections of α- and β-NAT (HNO3 · 3H2O) in the range 170 to 185 K and of metastable NAD (HNO3 · 2H2O) in the range 172 to 182 K, Journal of Geophysical Research: Atmospheres, 120, 11,707-11,727, https://doi.org/10.1002/2015JD023903, 2015.

Iraci, L. T., Middlebrook, A. M., and Tolbert, M. A.: Laboratory studies of the formation of polar stratospheric clouds: Nitric acid condensation on thin sulfuric acid films, Journal of Geophysical Research: Atmospheres, 100, 20969–20977, https://doi.org/10.1029/95JD02267, 1995.

Junge, C. E., Chagnon, C. W., and Manson, J. E.: STRATOSPHERIC AEROSOLS, Journal of Atmospheric Sciences, 18, 81–108, https://doi.org/https://doi.org/10.1175/1520-0469(1961)018<0081:SA>2.0.CO;2, 1961.

Kessenich, H. E., Seppälä, A., and Rodger, C. J.: Potential drivers of the recent large Antarctic ozone holes, Nature Communications 2023 14:1, 14, 1–9, https://doi.org/10.1038/s41467-023-42637-0, 2023.

Khaykin, S., Legras, B., Bucci, S., Sellitto, P., Isaksen, L., Tence, F., Bekki, S., Bourassa, A., Rieger, L., and Zawada, D.: The 2019/20 Australian wildfires generated a persistent smoke-charged vortex rising up to 35 km altitude, Commun Earth Environ, 1, 1–12, 2020.

Khosrawi, F., Urban, J., Pitts, M. C., Voelger, P., Achtert, P., Kaphlanov, M., Santee, M. L., Manney, G. L., Murtagh, D., and Fricke, K. H.: Denitrification and polar stratospheric cloud formation during the Arctic winter 2009/2010, Atmos Chem Phys, 11, 8471–8487, https://doi.org/10.5194/ACP-11-8471-2011, 2011.

Khosrawi, F., Urban, J., Lossow, S., Stiller, G., Weigel, K., Braesicke, P., Pitts, M. C., Rozanov, A., Burrows, J. P., and Murtagh, D.: Sensitivity of polar stratospheric cloud formation to changes in water vapour and temperature, Atmos Chem Phys, 16, 101–121, https://doi.org/10.5194/ACP-16-101-2016, 2016.

Klekociuk, A. R., Tully, M. B., Krummel, P. B., Henderson, S. I., Smale, D., Querel, R., Nichol, S., Alexander, S. P., Fraser, P. J., and Nedoluha, G.: The Antarctic ozone hole during 2020, Journal of Southern Hemisphere Earth Systems Science, 72, 19–37, https://doi.org/10.1071/ES21015, 2022.

Koop, T., Biermann, U. M., Raber, W., Luo, B. P., Crutzen, P. J., and Peter, T.: Do stratospheric aerosol droplets freeze above the ice frost point?, Geophys Res Lett, 22, 917–920, https://doi.org/10.1029/95GL00814, 1995.

Koop, T., Luo, B., Biermann, U. M., Crutzen, P. J., and Peter, T.: Freezing of HNO3/H2SO4/H2O Solutions at Stratospheric Temperatures: Nucleation Statistics and Experiments, J Phys Chem A, 101, 1117–1133, https://doi.org/10.1021/jp9626531, 1997.

Koop, T., Ng, H. P., Molina, L. T., and Molina, M. J.: A New Optical Technique to Study Aerosol Phase Transitions: The Nucleation of Ice from H2SO4 Aerosols, J Phys Chem A, 102, 8924–8931, https://doi.org/10.1021/jp9828078, 1998.

Koop, T., Luo, B., Tsias, A., and Peter, T.: Water activity as the determinant for homogeneous ice nucleation in aqueous solutions, Nature 2000 406:6796, 406, 611–614, https://doi.org/10.1038/35020537, 2000.

Lambert, A., Santee, M. L., Wu, D. L., and Chae, J. H.: A-train CALIOP and MLS observations of early winter Antarctic polar stratospheric clouds and nitric acid in 2008, Atmos Chem Phys, 12, 2899–2931, https://doi.org/10.5194/ACP-12-2899-2012, 2012.

Lambert, A., Santee, M. L., and Livesey, N. J.: Interannual variations of early winter Antarctic polar stratospheric cloud formation and nitric acid observed by CALIOP and MLS, Atmos Chem Phys, 16, 15219–15246, https://doi.org/10.5194/ACP-16-15219-2016, 2016.

Larsen, N., Knudsen, B. M., Rosen, J. M., Kjome, N. T., Neuber, R., and Kyrö, E.: Temperature histories in liquid and solid polar stratospheric cloud formation, Journal of Geophysical Research: Atmospheres, 102, 23505–23517, https://doi.org/10.1029/97JD01666, 1997.

Li, M., Shen, F., and Sun, X.: 2019–2020 Australian bushfire air particulate pollution and impact on the South Pacific Ocean, Scientific Reports 2021 11:1, 11, 1–13, https://doi.org/10.1038/s41598-021-91547-y, 2021.

Liu, G., Hirooka, T., Eguchi, N., and Krüger, K.: Dynamical evolution of a minor sudden stratospheric warming in the Southern Hemisphere in 2019, Atmos Chem Phys, 22, 3493–3505, https://doi.org/10.5194/ACP-22-3493-2022, 2022.

Lowe, D. and MacKenzie, A. R.: Polar stratospheric cloud microphysics and chemistry, J Atmos Sol Terr Phys, 70, 13–40, https://doi.org/10.1016/J.JASTP.2007.09.011, 2008.

Luo, B., Peter, T., and Crutzen, P.: Freezing of stratospheric aerosol droplets, Geophys Res Lett, 21, 1447–1450, https://doi.org/10.1029/93GL03076, 1994.

Luo, B. P., Voigt, C., Fueglistaler, S., and Peter, T.: Extreme NAT supersaturations in mountain wave ice PSCs: A clue to NAT formation, Journal of Geophysical Research: Atmospheres, 108, 4441, https://doi.org/10.1029/2002JD003104, 2003.

Mansoor, S., Farooq, I., Kachroo, M. M., Mahmoud, A. E. D., Fawzy, M., Popescu, S. M., Alyemeni, M. N., Sonne, C., Rinklebe, J., and Ahmad, P.: Elevation in wildfire frequencies with respect to the climate change, J Environ Manage, 301, 113769, https://doi.org/10.1016/J.JENVMAN.2021.113769, 2022.

Marti, J. and Mauersberger, K.: A survey and new measurements of ice vapor pressure at temperatures between 170 and 250K, Geophys Res Lett, 20, 363–366, https://doi.org/10.1029/93GL00105, 1993.

Molina, M. J. and Rowland, F. S.: Stratospheric sink for chlorofluoromethanes: chlorine atom-catalysed destruction of ozone, Nature, 249, 810–812, 1974.

Molina, M. J., Zhang, R., Wooldridge, P. J., McMahon, J. R., Kim, J. E., Chang, H. Y., and Beyer, K. D.: Physical chemistry of the H2SO4/HNO 3/H2O system: Implications for polar stratospheric clouds, Science (1979), 261, 1418–1423, https://doi.org/10.1126/SCIENCE.261.5127.1418, 1993a.

Molina, M. J., Zhang, R., Wooldridge, P. J., McMahon, J. R., Kim, J. E., Chang, H. Y., and Beyer, K. D.: Physical chemistry of the H2SO4/HNO3/H2O system: Implications for polar stratospheric clouds, Science (1979), 261, 1418–1423, 1993b.

Müller, R., Crutzen, P. J., Grooß, J.-U., Brühl, C., Russell III, J. M., and Tuck, A. F.: Chlorine activation and ozone depletion in the Arctic vortex: Observations by the Halogen Occultation Experiment on the Upper Atmosphere Research Satellite, Journal of Geophysical Research: Atmospheres, 101, 12531–12554, https://doi.org/https://doi.org/10.1029/95JD00220, 1996.

Müller, R., Crutzen, P. J., Grooβ, J.-U., Bürhl, C., Russell, J. M., Gernandt, H., McKenna, D. S., and Tuck, A. F.: Severe chemical ozone loss in the Arctic during the winter of 1995–96, Nature, 389, 709–712, https://doi.org/10.1038/39564, 1997.

Murphy, D. M., Froyd, K. D., Schwarz, J. P., and Wilson, J. C.: Observations of the chemical composition of stratospheric aerosol particles, Quarterly Journal of the Royal Meteorological Society, 140, 1269–1278, 2014.

Ohneiser, K., Ansmann, A., Kaifler, B., Chudnovsky, A., Barja, B., Knopf, D. A., Kaifler, N., Baars, H., Seifert, P., Villanueva, D., Jimenez, C., Radenz, M., Engelmann, R., Veselovskii, I., and Zamorano, F.: Australian wildfire smoke in the stratosphere: the decay phase in 2020/2021 and impact on ozone depletion, Atmos. Chem. Phys., 22, 7417–7442, https://doi.org/10.5194/acp-22-7417-2022, 2022.

Peter, T.: MICROPHYSICS AND HETEROGENEOUS CHEMISTRY OF POLAR STRATOSPHERIC CLOUDS, https://doi.org/10.1146/annurev.physchem.48.1.785, 48, 785–822, https://doi.org/10.1146/ANNUREV.PHYSCHEM.48.1.785, 1997.

Peter, T. and Grooß, J.-U.: Stratospheric ozone depletion and climate change, Royal Society of Chemistry, 108–144 pp., 2012.

Pitts, M. C., Thomason, L. W., Poole, L. R., and Winker, D. M.: Characterization of polar stratospheric clouds with spaceborne lidar: CALIPSO and the 2006 antarctic season, Atmos Chem Phys, 7, 5207–5228, https://doi.org/10.5194/ACP-7-5207-2007, 2007.

Pitts, M. C., Poole, L. R., and Thomason, L. W.: CALIPSO polar stratospheric cloud observations: Second-generation detection algorithm and composition discrimination, Atmos Chem Phys, 9, 7577–7589, https://doi.org/10.5194/ACP-9-7577-2009, 2009.

Pitts, M. C., Poole, L. R., Därnbrack, A., and Thomason, L. W.: The 2009-2010 Arctic polar stratospheric cloud season: A CALIPSO perspective, Atmos Chem Phys, 11, 2161–2177, https://doi.org/10.5194/ACP-11-2161-2011, 2011.

Pitts, M. C., Poole, L. R., Lambert, A., and Thomason, L. W.: An assessment of CALIOP polar stratospheric cloud composition classification, Atmos Chem Phys, 13, 2975–2988, https://doi.org/10.5194/ACP-13-2975-2013, 2013.

Ploeger, F., Diallo, M., Charlesworth, E., Konopka, P., Legras, B., Laube, J. C., Grooß, J.-U., Günther, G., Engel, A., and Riese, M.: The stratospheric Brewer–Dobson circulation inferred from age of air in the ERA5 reanalysis, Atmos Chem Phys, 21, 8393–8412, 2021.

Ravishankara, A. R. and Hanson, D. R.: Differences in the reactivity of type I polar stratospheric clouds depending on their phase, Journal of Geophysical Research: Atmospheres, 101, 3885–3890, https://doi.org/10.1029/95JD03009, 1996a.

Ravishankara, A. R. and Hanson, D. R.: Differences in the reactivity of type I polar stratospheric clouds depending on their phase, Journal of Geophysical Research: Atmospheres, 101, 3885–3890, 1996b.

Rex, M., Salawitch, R. J., von der Gathen, P., Harris, N. R. P., Chipperfield, M. P., and Naujokat, B.: Arctic ozone loss and climate change, Geophys Res Lett, 31, 2004.

Rieger, L. A., Randel, W. J., Bourassa, A. E., and Solomon, S.: Stratospheric temperature and ozone anomalies associated with the 2020 Australian New Year Fires, Geophys Res Lett, 48, e2021GL095898, 2021.

Robrecht, S., Vogel, B., Grooß, J. U., Rosenlof, K., Thornberry, T., Rollins, A., Krämer, M., Christensen, L., and Müller, R.: Mechanism of ozone loss under enhanced water vapour conditions in the mid-latitude lower stratosphere in summer, Atmos Chem Phys, 19, 5805–5833, https://doi.org/10.5194/ACP-19-5805-2019, 2019.

Santee, M. L., Lambert, A., Manney, G. L., Livesey, N. J., Froidevaux, L., Neu, J. L., Schwartz, M. J., Millán, L. F., Werner, F., Read, W. G., Park, M., Fuller, R. A., and Ward, B. M.: Prolonged and Pervasive Perturbations in the Composition of the Southern Hemisphere Midlatitude Lower Stratosphere From the Australian New Year's Fires, Geophys Res Lett, 49, e2021GL096270, https://doi.org/10.1029/2021GL096270, 2022a.

Santee, M. L., Lambert, A., Manney, G. L., Livesey, N. J., Froidevaux, L., Neu, J. L., Schwartz, M. J., Millán, L. F., Werner, F., Read, W. G., Park, M., Fuller, R. A., and Ward, B. M.: Prolonged and Pervasive Perturbations in the Composition of the Southern Hemisphere Midlatitude Lower Stratosphere From the Australian New Year's Fires, Geophys Res Lett, 49, e2021GL096270, https://doi.org/https://doi.org/10.1029/2021GL096270, 2022b.

Schneider, J., Weigel, R., Klimach, T., Dragoneas, A., Appel, O., Hünig, A., Molleker, S., Köllner, F., Clemen, H.-C., and Eppers, O.: Aircraft-based observation of meteoric material in lower-stratospheric aerosol particles between 15 and 68 N, Atmos Chem Phys, 21, 989–1013, 2021.

Schoeberl, M. R., Jensen, E. J., Pfister, L., Ueyama, R., Avery, M., and Dessler, A. E.: Convective Hydration of the Upper Troposphere and Lower Stratosphere, Journal of Geophysical Research: Atmospheres, 123, 4583–4593, https://doi.org/10.1029/2018JD028286, 2018.

Schwartz, M. J., Santee, M. L., Pumphrey, H. C., Manney, G. L., Lambert, A., Livesey, N. J., Millán, L., Neu, J. L., Read, W. G., and Werner, F.: Australian new year's pyrocb impact on stratospheric composition, Geophys Res Lett, 47, e2020GL090831, 2020.

Sellitto, P., Belhadji, R., Kloss, C., and Legras, B.: Radiative impacts of the Australian bushfires 2019–2020–Part 1: Large-scale radiative forcing, EGUsphere, 1–20, 2022.

Solomon, S., Dube, K., Stone, K., Yu, P., Kinnison, D., Toon, O. B., Strahan, S. E., Rosenlof, K. H., Portmann, R., Davis, S., Randel, W., Bernath, P., Boone, C., Bardeen, C. G., Bourassa, A., Zawada, D., and Degenstein, D.: On the stratospheric chemistry of midlatitude wildfire smoke, Proc Natl Acad Sci U S A, 119, e2117325119, https://doi.org/10.1073/PNAS.2117325119/SUPPL_FILE/PNAS.2117325119.SAPP.PDF, 2022.

Stocker, M., Ladstädter, F., and Steiner, A. K.: Observing the climate impact of large wildfires on stratospheric temperature, Sci Rep, 11, 22994, https://doi.org/10.1038/s41598-021-02335-7, 2021.

Tabazadeh, A., Turco, R. P., Drdla, K., Jacobson, M. Z., and Toon, O. B.: A study of type I polar stratospheric cloud formation, Geophys Res Lett, 21, 1619–1622, 1994.

Taha, G., Loughman, R., Zhu, T., Thomason, L., Kar, J., Rieger, L., and Bourassa, A.: OMPS LP Version 2.0 multi-wavelength aerosol extinction coefficient retrieval algorithm, Atmos Meas Tech, 14, 1015–1036, https://doi.org/10.5194/AMT-14-1015-2021, 2021.

Tencé, F., Jumelet, J., Sarkissian, A., Bekki, S., and Khaykin, S.: Optical properties of smoke particules from Australian 2019-20 wildfires derived from lidar measurements at the French Antarctic station Dumont d'Urville, in: EGU General Assembly Conference Abstracts, EGU21-12466, 2021.

Tencé, F., Jumelet, J., Bekki, S., Khaykin, S., Sarkissian, A., and Keckhut, P.: Australian Black Summer Smoke Observed by Lidar at the French Antarctic Station Dumont d'Urville, Journal of Geophysical Research: Atmospheres, 127, e2021JD035349, https://doi.org/10.1029/2021JD035349, 2022.

Thölix, L., Backman, L., Kivi, R., and Karpechko, A. Y.: Variability of water vapour in the Arctic stratosphere, Atmos Chem Phys, 16, 4307–4321, https://doi.org/10.5194/ACP-16-4307-2016, 2016.

Thomason, L. W. and Peter, T.: Assessment of stratospheric aerosol properties (ASAP), SPARC report, 2006.

Toon, O. B., Turco, R. P., Jordan, J., Goodman, J., and Ferry, G.: Physical processes in polar stratospheric ice clouds, Journal of Geophysical Research: Atmospheres, 94, 11359–11380, 1989.

Tritscher, I., Pitts, M. C., Poole, L. R., Alexander, S. P., Cairo, F., Chipperfield, M. P., Grooß, J. U., Höpfner, M., Lambert, A., Luo, B., Molleker, S., Orr, A., Salawitch, R., Snels, M., Spang, R., Woiwode, W., and Peter, T.: Polar Stratospheric Clouds: Satellite Observations, Processes, and Role in Ozone Depletion, Reviews of Geophysics, 59, e2020RG000702, https://doi.org/10.1029/2020RG000702, 2021.

Voigt, C., Schreiner, J., Kohlmann, A., Zink, P., Mauersberger, K., Larsen, N., Deshler, T., Kroger, C., Rosen, J., and Adriani, A.: Nitric acid trihydrate (NAT) in polar stratospheric clouds, Science (1979), 290, 1756–1758, 2000.

Voigt, C., Schlager, H., Luo, B. P., Dörnbrack, A., Roiger, A., Stock, P., Curtius, J., Vössing, H., Borrmann, S., and Davies, S.: Nitric acid trihydrate (NAT) formation at low NAT supersaturation in polar stratospheric clouds (PSCs), Atmos Chem Phys, 5, 1371–1380, 2005.

Voigt, C., Dörnbrack, A., Wirth, M., Groß, S. M., Pitts, M. C., Poole, L. R., Baumann, R., Ehard, B., Sinnhuber, B. M., Woiwode, W., and Oelhaf, H.: Widespread polar stratospheric ice clouds in the 2015-2016 Arctic winter - Implications for ice nucleation, Atmos Chem Phys, 18, 15623–15641, https://doi.org/10.5194/ACP-18-15623-2018, 2018.

Waibel, A. E., Peter, T., Carslaw, K. S., Oelhaf, H., Wetzel, G., Crutzen, P. J., Poschl, U., Tsias, A., Reimer, E., and Fischer, H.: Arctic ozone loss due to denitrification, Science (1979), 283, 2064–2069, 1999.

Wang, P., Solomon, S., and Stone, K.: Stratospheric chlorine processing after the 2020 Australian wildfires derived from satellite data, Proc Natl Acad Sci U S A, 120, e2213910120, https://doi.org/10.1073/PNAS.2213910120/SUPPL_FILE/PNAS.2213910120.SAPP.PDF, 2023.

Weiss, F., Kubel, F., Gálvez, Ó., Hoelzel, M., Parker, S. F., Baloh, P., Iannarelli, R., Rossi, M. J., and Grothe, H.: Metastable Nitric Acid Trihydrate in Ice Clouds, Angewandte Chemie International Edition, 55, 3276–3280, https://doi.org/10.1002/ANIE.201510841, 2016.

Yook, S., Thompson, D. W. J., and Solomon, S.: Climate Impacts and Potential Drivers of the Unprecedented Antarctic Ozone Holes of 2020 and 2021, Geophys Res Lett, 49, e2022GL098064, https://doi.org/https://doi.org/10.1029/2022GL098064, 2022.

Yu, P., Davis, S. M., Toon, O. B., Portmann, R. W., Bardeen, C. G., Barnes, J. E., Telg, H., Maloney, C., and Rosenlof, K. H.: Persistent stratospheric warming due to 2019–2020 Australian wildfire smoke, Geophys Res Lett, 48, e2021GL092609, 2021.

Zhang, R., Leu, M., and Keyser, L. F.: Hydrolysis of N2O5 and ClONO2 on the H2SO4/HNO3/H2O ternary solutions under stratospheric conditions, Geophys Res Lett, 22, 1493–1496, 1995.

Zhu, Y., Toon, O. B., Kinnison, D., Harvey, V. L., Mills, M. J., Bardeen, C. G., Pitts, M., Bègue, N., Renard, J. B., Berthet, G., and Jégou, F.: Stratospheric Aerosols, Polar Stratospheric Clouds, and Polar Ozone Depletion After the Mount Calbuco Eruption in 2015, Journal of Geophysical Research: Atmospheres, 123, 12,308-12,331, https://doi.org/10.1029/2018JD028974, 2018.